Geological Magazine

www.cambridge.org/geo

Syndepositional processes in the pigmentation of oceanic red beds: evidence from the Basque–Cantabrian Basin (northern Spain)

Javier Elorza[1], Juan José Gómez-Alday[2] and Álvaro Jiménez Berrocoso[3]

[1]Dpto. Mineralogía y Petrología. Universidad del País Vasco. Apartado 644; 48080 Bilbao, Spain; [2]Grupo Hidrogeología. IDR. Universidad Castilla-La Mancha. 02071 Albacete, Spain and [3]Repsol Exploration, c/Méndez Álvaro 44, 28045 Madrid, Spain

Original Article

Cite this article: Elorza J, Gómez-Alday JJ, and Jiménez Berrocoso Á (2021) Syndepositional processes in the pigmentation of oceanic red beds: evidence from the Basque–Cantabrian Basin (northern Spain). *Geological Magazine* **158**: 1683–1703. https://doi.org/10.1017/S0016756821000248

Received: 13 June 2020
Revised: 14 February 2021
Accepted: 11 March 2021
First published online: 13 April 2021

Keywords:
oceanic red beds; calcareous couplets; oxygen and carbon isotopes; oxygen-rich water masses; Late Cretaceous; Paleocene; Basque–Cantabrian Basin

Author for correspondence: Javier Elorza, Email: josejavier.elorza@ehu.eus

Abstract

Oceanic red beds (ORBs) are present in Upper Cretaceous and Danian deep-marine deposits in the Basque–Cantabrian Basin of northern Spain. The presence and regularity of the succession of marl–limestone couplets is exceptional based on the macroscopic, microscopic and geochemical evidence collected. Five types of marl–limestone couplets are identified based on the colour, and a high maximum sedimentation rate (3.6 cm ka^{-1}) is noted. The oxidizing activity of deep, cold-water masses is indicated by the oxygen isotope signal in the lower–upper Maastrichtian and Danian sections and the presence of the boreal inoceramid *Spyridoceramus tegulatus*. In theory, the variation in colour from grey to greenish-yellow, purple and pink up to red tones correlates with the $Fe^{2+}/(Fe^{2+}+Fe^{3+})$ ratio. It is interpreted as the possible palaeoenvironmental transit of particles that sediment out slowly in oxic environments when they circulate through cooler, oxidizing water masses. The colour is considered to be a depositional feature, and hematite, detected by X-ray diffraction, is the main staining agent, without discarding the possible redistribution of previous oxyhydroxides passing to hematite as a final product. The cell filling of the foraminifer shells does not incorporate appreciable amounts of Fe and Mg during diagenesis. Bacterial activity is detected using scanning electron microscopy images, both in the coccolith debris and in the detrital micas, although there is uncertainty as to its importance in the staining process.

1. Introduction

The geological history of the Cretaceous Period is marked by stages during which deep-marine environments underwent major deposition and burial of organic-rich, fine-grained sediments (referred to here as black shales) at regional to basin scales under the influence of low-to-absent dissolved oxygen in seawater (Hsü & Jenkyns, 1974; Schlanger & Jenkyns, 1976; Scholle & Arthur, 1980; Weissert *et al.* 1985; Jenkyns, 2010; Hüneke & Mulder, 2011). These periods have been called ocean anoxic events (OAEs), and it is generally accepted that at least five major OAEs occurred during the Cretaceous Period (Schlanger & Jenkyns, 1976; Jenkyns, 1980, 2010; Arthur *et al.* 1990; Wilson & Norris, 2001; Jarvis *et al.* 2006; Najarro *et al.* 2011; Beil *et al.* 2019). Cretaceous OAEs took place during greenhouse conditions (i.e. warm temperatures globally and high atmospheric pCO_2), and their major significance is that they deeply perturbed the global carbon cycle through feedback mechanisms that controlled the evolution of the ocean–climate system. These events are also characterized by positive carbon isotope ($\delta^{13}C$) excursions related to globally enhanced rates of organic carbon burial. The intervals between Cretaceous OAEs, albeit still greenhouse conditions, are considered to be normal periods of comparatively increased seawater oxygenation and temperature change (Jenkyns, 2010; Robinson *et al.* 2017). However, it is generally recognized that the global temperature established in OAE2 (except for the Plenus Cold Event) was prevalent until the early Turonian Age due to the high CO_2 content, meaning that the subsequent cooling required changes in other factors such as a rise in sea level, weathered silicate rocks and/or nutrient sequestration in black shales (Robinson *et al.* 2019).

In contrast to the Cretaceous OAEs, in subsequent periods oxic, deep-marine sediments were deposited in the world's oceans, including red to pink to purple/green/yellow limestones, marlstones, claystones and cherts (Hu *et al.* 2005; Scott, 2009). These sediments have been called Cretaceous oceanic red beds (ORBs) (Wang *et al.* 2004, 2005; Hu *et al.* 2005) and, because they followed OAEs, many studies consider that their deposition was an inevitable consequence of OAE conditions (Wagreich *et al.* 2009; Wang *et al.* 2011). That is, continued organic-rich deposition during OAEs represented a CO_2 sink, a situation that subsequently allowed both atmospheric oxygen and seawater-dissolved oxygen to increase, thus leading to the sedimentation of Cretaceous ORBs (Wagreich *et al.* 2009; Wang *et al.* 2011; Gambacorta *et al.* 2016).

CAMBRIDGE UNIVERSITY PRESS

Along with oxygenated water masses, the main accepted conditions for the formation of Cretaceous ORBs are low sedimentation rates and oligotrophic conditions in seawater (Scott, 2009). In general, low sedimentation rates in an oxygenated water column would provide enough time for the oxidation of seawater Fe^{2+} into Fe^{3+} as the main colouring agent in ORBs, the precipitation of Fe^{3+}-rich oxides in the water colum and/or within the sediments (surrounding other particles in both cases), and the incorporation of Fe^{3+} into the crystal structure of carbonate minerals (e.g. calcite) (Jansa & Hu, 2009; Hu *et al.* 2012). Oligotrophic conditions, with a very low level of nutrients, imply that only small amounts of organic matter would reach the seafloor; this situation would promote its rapid degradation, reducing the likelihood of the creation of low-oxygen conditions in bottom waters and/or within the sediments.

The Upper Cretaceous and Paleocene sediments of the Basque–Cantabrian Basin in northern Spain are well suited for studying the origin of the colour variations within ORBs. Of particular interest are a series of short succesions (2–5 m thick) from the lower Turonian, lower Maastrichtian, upper Maastrichtian and Danian sediments that were deposited in deep-marine environments, at a palaeodepth of at least 1500 m (Pujalte *et al.* 1998), in the Western Tethys facing the open North Atlantic. The sections are biostratigraphically complete with easily accessible outcrops that have traditionally provided a wealth of lithological, palaeontological, geochemical and cyclostratigraphic information (Gómez-Alday *et al.* 2004, 2008; Dinarès-Turrell *et al.* 2013). Here, we describe the details of these colour variations, interpret their possible origin and discuss their palaeoceanographic significance. A broader impact of our work is that it may help to understand the products of the interaction between ocean and climate under greenhouse conditions, which has implications for our understanding of the evolution of our current climate.

2. Geological setting and antecedents

The Basque–Cantabrian Basin is located in the westernmost part of the Pyrenean chain, and its depositional history is connected to the opening of the Bay of Biscay (Fig. 1a–c). This basin constituted the most northerly part of the central North Iberian margin and occupied a latitude of *c.* 30–35°N during most of the Late Cretaceous–Paleocene epochs (Rat *et al.* 1983; Plaziat, 1981; Floquet, 2004). A deep-marine sector, the so-called Basque Arc Domain, with several sub-basins (e.g. the Plentzia and San Juan de Luz troughs) experienced a high rate of subsidence and the deposition of more than 4000 m of calcareous flysch during the Cenomanian–Santonian ages (Mathey, 1987). The deep-marine sector was connected to platform settings to the south and SW (North Iberian platform) and NE (Aquitaine platform), which underwent lower subsidence rates and accumulated *c.* 1000 m of mainly carbonates (Floquet, 2004).

In recent decades there have been many studies, with very diverse objectives, carried out on materials in flysch facies that make up the Upper Cretaceous and Palaeogene strata of the Basque–Cantabrian Basin (Martín Chivelet *et al.* 2002; Baceta *et al.* 2004; Floquet, 2004), collected in *The Geology of Spain* (Gibbons & Moreno, 2002) and *Geología de España* (Vera, 2004). However, although the different colours of the same flysch facies are mentioned explicitly, as far as we know the process that gives rise to their colour, and therefore the ORB occurrence in the Basque Arc Domain, has not been investigated in depth as has been done in the North Atlantic, Eastern Alps and Carpathian areas (Wang *et al.* 2011; Cai *et al.* 2012; Hu *et al.* 2012). In short educational works published with students at the University of the Basque Country, general ideas have been propounded on the local presence of the Cretaceous ORBs, which extend to the Danian Stage, as well as on the palaeoenvironmental conditions that would have favoured the red, greenish-yellow and pink colours in short sections where these facies are exposed (Domínguez *et al.* 2007; Santander *et al.* 2007; Alonso de Linaje *et al.* 2009; Iridoy *et al.* 2010).

3. Selected sections

Representative sections of red facies that emerge in the Basque Arc Domain (Fig. 1a, c) have been chosen: (1) the lower Turonian cliffs of Muriola beach (Fig. 2a); (2) five sections in the lower Maastrichtian (Fig. 3a) and upper Maastrichtian (Figs 4a and 5a) Sopelana beach cliffs; and (3) Danian materials (Fig. 6a).

3.a. Muriola beach cliff: Lower Turonian section

The Muriola beach sea-cliff exposure (Barrika village, 20 km NE of Bilbao) covers less than 80 m and is assigned to the basal Plentzia Formation (middle Cenomanian – uppermost Santonian; Mathey, 1982); it is well developed on the NE flank of the Biscay Synclinorium, with a local direction of N90°E (Fig. 1a, c). In general, the Plentzia Formation is formed of grey carbonate turbidites where the central part contains bedded and nodular chert in the Tb, Tc and Td intervals of the Bouma sequence (Elorza & Bustillo, 1989), but the Muriola beach section contains a dysoxic–anoxic event (1.40 m thick, expanded by 0.50 m of interbedded turbidites) that is the OAE2 itself or a local anoxic episode (Fig. 2a). Above and a short distance away, as a result of the presence of faults, a small deposit of reddish hemipelagic marls (> 2 m thick) has thin, interbedded grey turbidites that likely formed in a deep basin environment (Fig. 2b, c). Planktonic foraminifer species (*Marginotruncana pseudolinneaina*, *Marginotruncana renzi*, *Helvetoglobotruncana praehelvetica*, *Dicarinella hagni* and *Dicarinella canaliculata*) date this section as early Turonian age. The thin grey turbiditic beds include trace fossils at the base, but do not contain macrofossils such as ammonite moulds or inoceramid debris. The existence of small normal faults with reactivation structures, stylolites and extension veins are highlighted.

3.b. Sopelana beach cliffs

The Sopelana beach (15 km NE of Bilbao) has a length of more than 800 m and its cliffs contain materials of different environments and ages, delimited by faults (Elorza *et al.* 1984). All the materials were folded by the Alpine Orogeny and make up the NE flank of the Biscay Synclinorium, with a general fold axis direction of N120°E. Palaeogeographic reconstructions situate the basin at latitude 30–35°N. The Maastrichtian sediments of the Basque Arc Domain were deposited in the Orio trough, formed during the Campanian Age and limited by the North Iberian platform to the south and the Aquitaine platform to the north (see Plaziat, 1981; Mathey, 1987; Pujalte *et al.* 1998, 2000). Gypsums, clays and volcanic rocks (Keuper Facies, Triassic) are visible to a minor extent compared with the vast extent of carbonate sediments ordered by couplets of marls with either marly limestone or limestone, corresponding to the lower and upper Maastrichtian Stage, included in the Zumaya–Algorri Formation (Mathey, 1982) and differentiated into Members I–V (MacLeod & Ward, 1990; Ward & Kennedy, 1993). Although the lower and upper Maastrichtian couplets usually comprise subcouplets of marls and marly limestones, for the sake of simplicity we refer to these as marl–limestone couplets. Small sections of interest are found in the Sopelana beach cliffs (Figs 1, 3–6): the lower Maastrichtian, upper Maastrichtian and Danian sections.

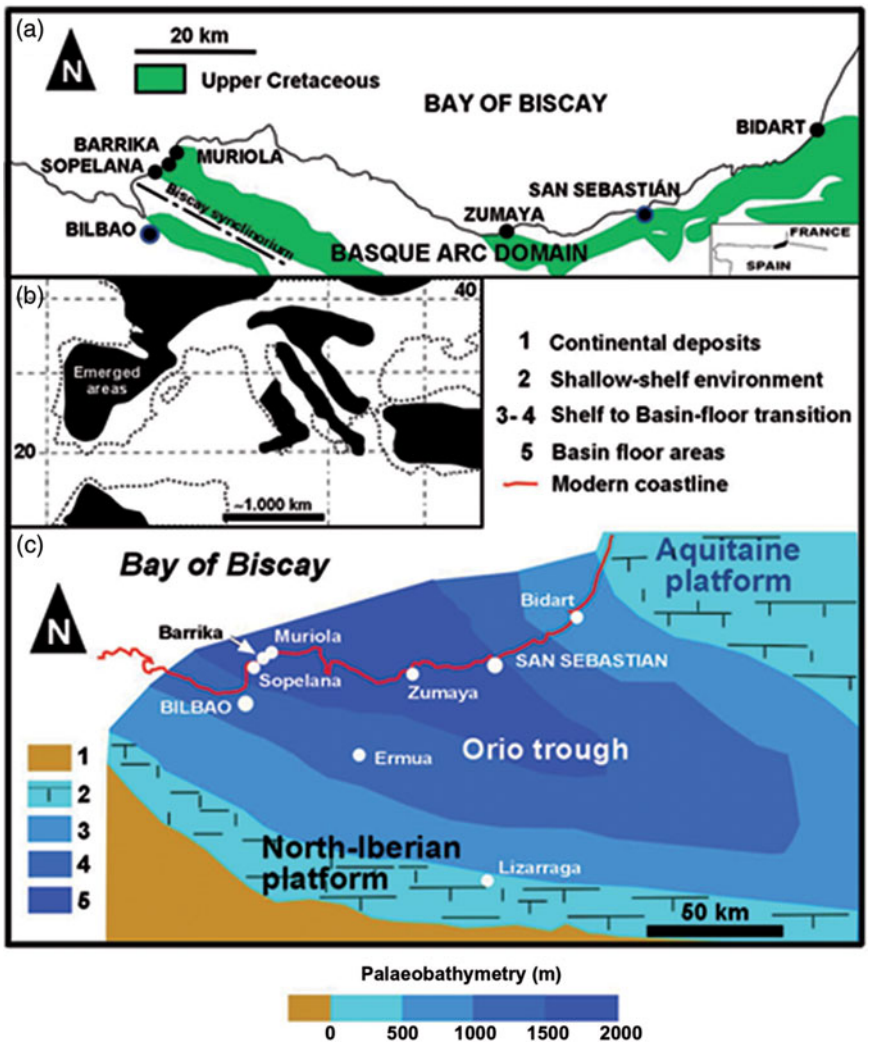

Fig. 1. (Colour online) (a) Simplified geological map of the northern part of the Basque Arc Domain showing the location of the Upper Cretaceous and Danian sections discussed (modified from Mathey, 1987). (b) Regional palaeogeography, according to Arenillas *et al.* (1998). (c) Simplified palaeogeographic sketch of the Basque–Cantabrian Basin in Maastrichtian times. Outlines show approximate palaeobathymetry, modified from Plaziat (1981), Mathey (1987) and Pujalte *et al.* (2000), together with the different sections and cities referred to in the text.

3.b.1. Lower Maastrichtian section

The materials of the lower Maastrichtian section are composed of grey marl–limestone couplets without turbiditic episodes and with a high rate of sedimentation per couplet (3 cm ka^{-1}); they were deposited in a deep basin environment (Gómez-Alday *et al.* 2004; Álvarez-Llano *et al.* 2006). The section belongs to the *Gansserina gansseri* biozone, in chron C31R prior to the latest Cretaceous regression. Macrofossils comprise thick, complete inoceramid shells (Ward *et al.* 1991; MacLeod, 1994; Gómez-Alday *et al.* 2004, 2008) and scarce ammonite moulds of different species (Ward & Kennedy, 1993), in addition to *Zoophycos* and *Planolites* as the dominant ichnofossils.

The object of our attention is a small section in the eastern part of Sopelana beach called El Peñón, where the carbonate marl–limestone couplets, inverted due to nearby diapiric activity, correspond to the lower Maastrichtian section of the Zumaya–Azgorri Formation (Fig. 3a). The marl–limestone couplets are mostly grey, with considerable large *Platyceramus salisburgensis* (Fugger & Kastner, 1885) (Fig. 3b) inoceramid shells. However, they evolve into greenish-yellow tones and then a greater prevalence of red tones (Fig. 3c, d). In these materials of greenish-yellow to reddish tones, inoceramid fragments, echinoids, trace fossils with numerous *Zoophycos* and later bleached fractures are preserved (Fig. 3b*, e–h).

3.b.2. Upper Maastrichtian section

Three small, complementary upper Maastrichtian sections have been chosen for this study. Section UM1 (2.67 m thick) is formed of six marl–limestone couplets of yellowish-grey shades in the limestones and slightly purple tones in the marls, arranged in normal position and belonging to the lower part of the upper Maastrichtian section (Fig. 4a, b). In the same Sopelana cliff, section UM1 has been complemented with another, smaller section, UM1*, of thicker couplets (two marl–limestone couplets, 1.39 m) with similar lithological characteristics and ichnofossil contents. Above, section UM2 (3.60 m thick) has five marl–limestone couplets of generally purple tones, both in marls and limestones (Fig. 4a, c, d). Both sections correspond to the *Abathomphalus mayaroensis* biozone, forming part of Member IV (Ward & Kennedy, 1993).

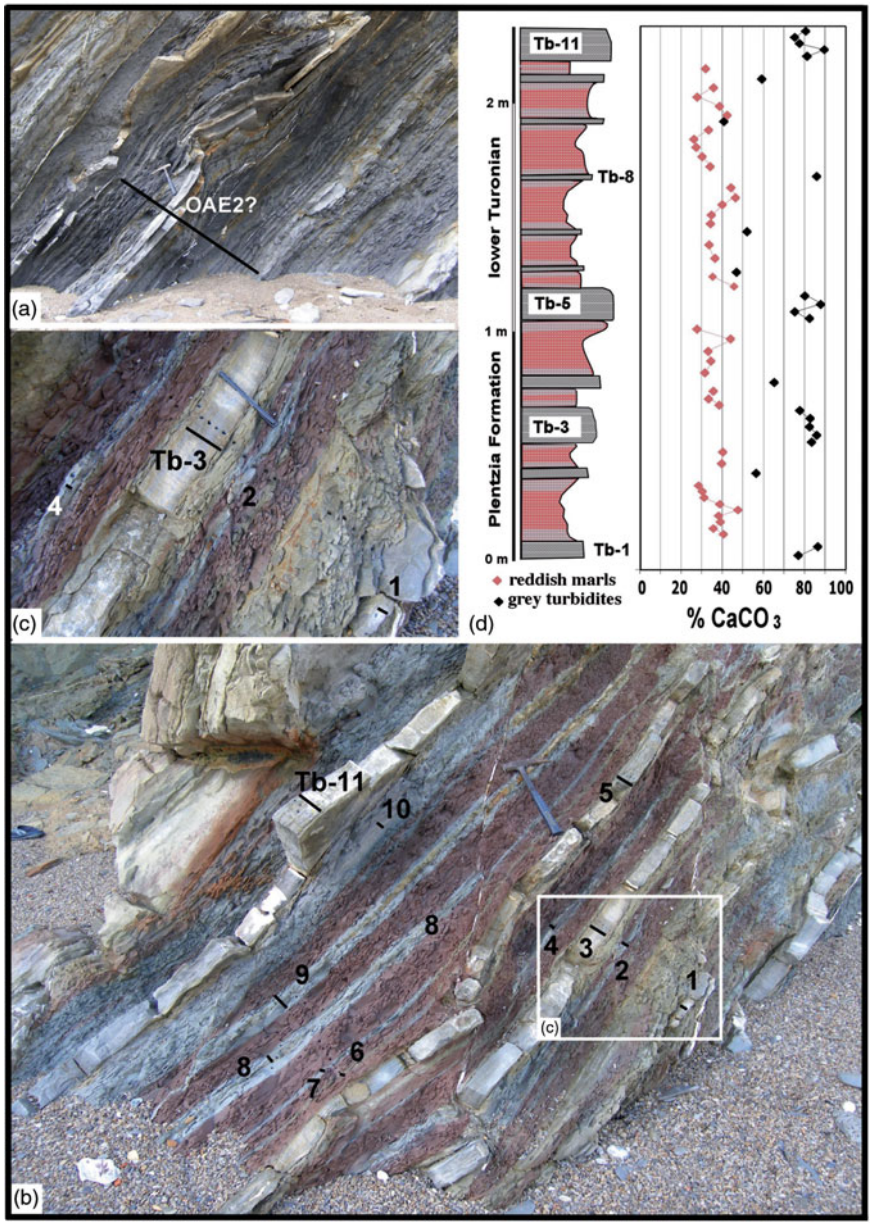

Fig. 2. (Colour online) Lower Turonian section (Muriola beach cliff). (a) View of the oceanic anoxic event (OAE2?) a few metres below the reddish marls. (b) Overview of the reddish hemipelagic marls with intercalated grey carbonate turbidites (Tb), belonging to the lower Turonian. (c) Detail of the reddish marls associated with grey carbonate turbidites, with irregular bleaching signs in the red marl–turbidite contact. The black bars and numbers indicate the sampling transect in the carbonate turbidites. (d) Stratigraphic column of the reddish marls, with grey carbonate turbidites. The lengths of the hammer and marker pen are 36 cm and 14 cm, respectively.

3.b.3. Danian section

The Paleocene sediments were deposited in slope-apron, basin-floor and deep-sea channel environments limited by the shallow limestones of the North Iberian platform to the south and the Aquitaine platform to the north. Neither purple nor intense red, the pink and white colour of the limestones is the most evident and defining characteristic in all recognized outcrops of Danian age (Sopelana, Zumaya, San Sebastián, Hendaye, Bidart sections) in the Basque Arc Domain (Fig. 1a). The small fragment of the stratigraphic record chosen in the Sopelana beach cliff belongs to the pinkish-white pelagic limestones and hemipelagic marls of the Danian (lower Palaeogene), located on the northeastern flank of the Biscay Synclinorium (Figs 1a, c, 4a, 6a, b).

The marl–limestone couplets are grouped in turn in sets in different ways (tight, amalgamated and open), without intervening turbiditic episodes or slides that would generate intraformational gaps. The depositional environment is deep basin and reaches the biozones of *Eoglobigerina pseudobulloides* and *Eoglobigerina trinidadensis* (Pujalte *et al.* 1998). The marl–limestone couplets are predominantly pink, but can change at the intrabed scale to white tones in both lithologies (Fig. 6c, e). Only crushed echinoid shells appear as macrofossils, and *Zoophycos* and *Planolites* are the predominant ichnofossils (Fig. 6g). The limestone subcouplets have numerous sutured, irregular small stylolites perpendicular to the stratification surface (Fig. 6h).

4. Methods

Detailed sedimentary logs, photographic documentation and a large sample set of bulk sediments and fossil shells from the sections studied

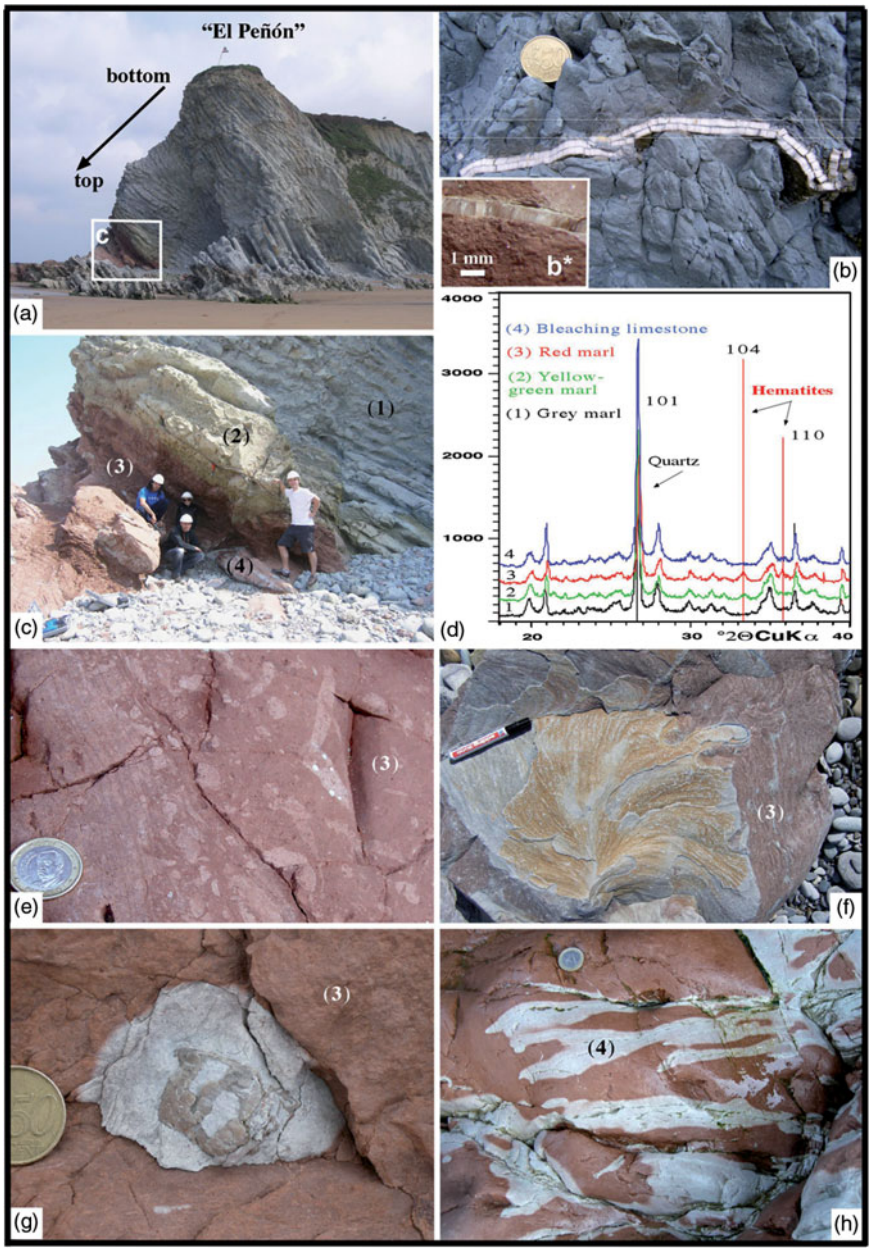

Fig. 3. (Colour online) (a) Inverted section called El Peñón of marl–limestone couplets belonging to the lower Maastrichtian (Sopelana beach cliffs). (b, b*) Longitudinal inoceramid section with a thick prismatic microstructure (> 6 mm) in the grey facies compared with the thin prismatic microstructure of the inoceramid (< 1 mm) in the red facies. (c) Detail of the inverted section where the gradual passage of grey (1) to yellowish-green (2) to red (3) couplets and finally to bleached (4) limestones is recognizable. (d) Diffractograms of grey marl (1), yellowish-green marl (2), red marl (3) and bleached limestone (4) showing a hematite composition (104 and 110 peaks) in the yellowish-green and red materials. (e) Detail of the heavy bioturbation in the red lithology (3), indicative of intense oxygenation. (f) View of a specimen of *Zoophycos* ichnofossil with clear changes in colouring (bleaching) included in red facies (3) of the same section. (g) View of an echinoid fossil causing a bleaching crown during the decomposition of organic matter in the red facies (3). (h) Network of irregular fractures as a means of transmission of reducing fluids, capable of bleaching a limited part (4) of the consolidated red limestone. Diameter of coin is (b, g) 2.4 cm and (e, h) 2.3 cm. (f) Pen is 13.5 cm long.

were collected over several field seasons. We examined more than 50 thin-sections by standard microscopy methods, using Alizarin Red S and potassium ferricyanide staining (Dickson, 1965). All cathodoluminescence (CL) work employed a Technosyn Cold Cathode Luminescence system (model 8200 Mk II) mounted on an Olympus trinocular research microscope with a maximum magnification capability of 400×, using universal stage objectives. Standard operating conditions included an accelerating potential of 12 kV and a 0.5–0.6 mA beam current with a beam diameter of approximately 5 mm. For the intervals specifically addressed in this paper, sampling resolution was increased up to 2 cm per sample. Samples were collected using a portable drill and 6 mm bits on fresh surfaces of marls, marly limestones and limestones. The proportion of $CaCO_3$ (in percent) was measured on a split (90–150 mg) of each powdered sample using an automated calcimeter (Aquitaine Technique Innovation, Bordeaux, France) at the University of the Basque Country (Bilbao, Spain) following the method of Bernard (Allison & Moodie, 1965). The pressure of the evolved CO_2 gas was individually measured and converted to % $CaCO_3$. Analytical precision is better than 4% on the basis of replicate analyses. The stable isotope data were obtained from the same samples at the University of Missouri (USA) by reacting *c.* 50 μg of powder in 103% H_3PO_4 at 70°C in a Kiel III carbonate device. The $\delta^{13}C$ and $\delta^{18}O$

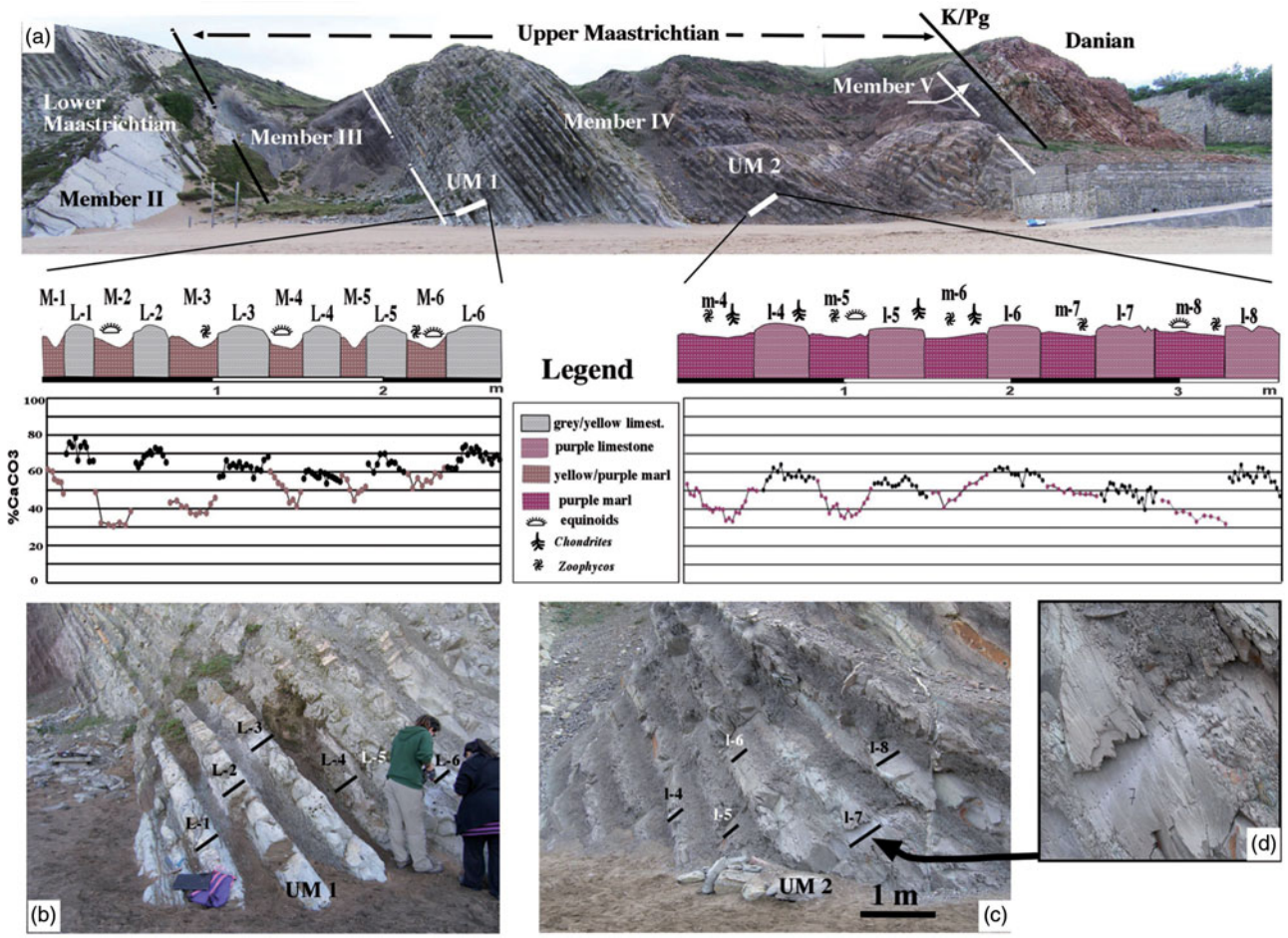

Fig. 4. (Colour online) (a) General view of the Sopelana cliffs with the lower Maastrichtian top part (Member II) and the upper Maastrichtian (Members III, IV and V) as far as the K/Pg limit followed by the development of the Danian pink marl–limestone couplets. The values in %$CaCO_3$ of the small sections UM1 and UM2 studied are incorporated, where the high compositional differences between the marl and limestone couplets in section UM1 are quite noticeable compared with the much more gradual changes in section UM2. (b, c) Complete views of section UM1 (grey-yellow limestone and purple marl) and section UM2 (purple limestone and purple marl) chosen to obtain %$CaCO_3$ values. (d) Detail of (c), where the step from marl to marly limestone is scarcely perceptible. Black bars and numbers point to the limestone subcouplets transect where samples were taken.

of the evolved CO_2 was determined online in a Thermo Finnegan Delta Plus mass spectrometer. The results are normalized to the average of multiple analyses of the NBS-19 standard. The resulting corrections were small, and analytical precision, based on uncorrected values for NBS-19, was 0.02‰ and 0.05‰ for $\delta^{13}C$ and $\delta^{18}O$, respectively. The isotope data are expressed in the standard δ-notation relative to the Vienna PDB standard.

A number of samples were selected and examined under a scanning electron microscope (SEM) and qualitatively determined (Al, Si, Fe, P, K, Ca) by energy-dispersive spectrometry (EDX) using a Jeol JSMT6400 at the University of the Basque Country. X-ray diffraction (XRD) analyses were performed with a Phillips PW1710 diffractometer using Cu Ka radiation monochromated by graphite with generator conditions of 40 kV, 20 mA, a step size of 0.02° (°2θ) and a time per step of 1 s.

5. Results

5.a. Lower Turonian section (Muriola beach cliff)

In the hemipelagic reddish marls of 2.35 m thickness, a total of 11 layers of grey carbonate turbidites Tb-1 to Tb-11 are intercalated, with parallel and cross laminations (Fig. 2b). The reddish marls are irregularly 'bleached' in contact with the grey turbidite beds (Fig. 2c). High-resolution calcimetric analyses (38 samples; *c.* 2–3 cm per sample) of the red hemipelagic marls reveal a mean value of 36% $CaCO_3$, whereas the mean value of the 23 samples of the grey carbonate turbidites is 75% $CaCO_3$ (Table 1).

In the turbidites Tb-3 and Tb-11, of medium thickness, a decrease in the concentration of $CaCO_3$ is observed towards the top (Fig. 2d). The analysis of red marls by XRD confirms that the minority mineral phases correspond to quartz, plagioclase, feldspar, micas and clays such as kaolinite and illite and/or smectite. The presence of hematite is recognized in the insoluble concentrate, as a result of the red marls having been attacked with dilute HCL. The chronostratigraphic and geochemical characteristics assign the reddish marls of Muriola beach to the Ca Cretaceous ORBs and as short-term Cretaceous ORBs of age < 1 Ma, according to the classification of Hu *et al.* (2012).

5.b. Lower Maastrichtian section (Sopelana beach cliff)

In El Peñón section, high-resolution calcimetric analysis provides a mean value across the five grey limestones of 79% $CaCO_3$ versus 60% for five grey marls; a mean value of 62% $CaCO_3$ for five greenish-yellow marls; 65% $CaCO_3$ for five red marls versus 87% for three red limestones; and a mean value of 91% $CaCO_3$ for three red

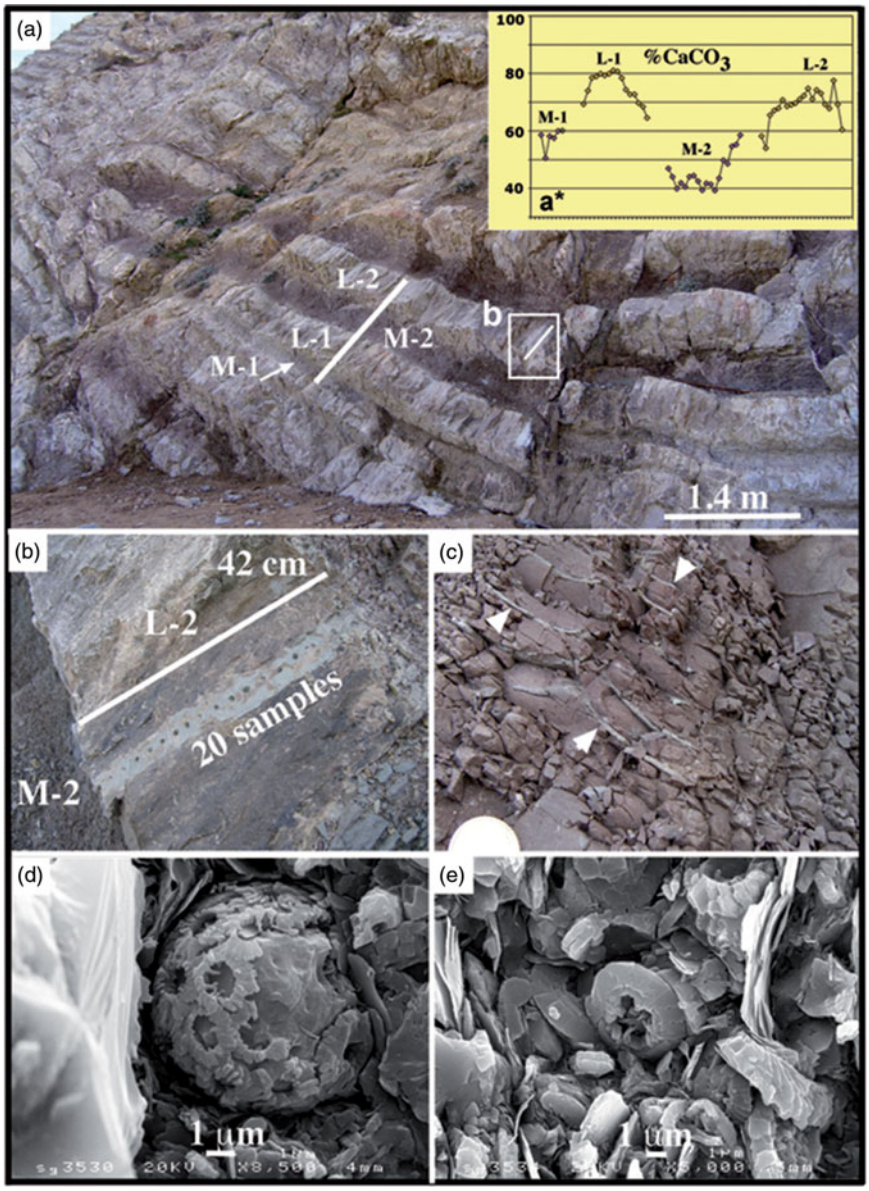

Fig. 5. (Colour online) (a) Upper Maastrichtian section UM1* where the marl–limestone couplets are very thick (central part of Sopelana beach cliffs). (a*) The marl subcouplets (M-1, -2) have purple tones whereas the limestone subcouplets (L-1, -2) have yellowish-grey tones. (b) Detail of transect for calcimetric analysis (2 cm per sample) of the yellowish-grey limestone subcouplet. (c) Detail of purple marl subcouplet with a vertical section of a *Zoophycos* fossil recognized by its bleached spreite whorls, indicated by the head of white arrows. Diameter of coin is 2.4 cm. (d, e) SEM views of a coccosphere and coccolith plates as calcareous nannoplankton and ferromagnesian clay remain protected and conserved in the *Zoophycos* cross-cut.

limestones with bleaching effect. These mean values indicate a high percentage of $CaCO_3$, although with a 20% difference between limestone versus marl values (Table 1). These compositional characteristics allow us to classify the reddish and greenish-yellow couplets of the lower Maastrichtian section as belonging to the Ca Cretaceous ORBs and as short-term Cretaceous ORBs of age < 1 Ma (Hu *et al.* 2012). The $\delta^{18}O‰$ and $\delta^{13}C‰$ (V-PDB) values of the same samples in the grey and red facies were obtained to provide complementary data (Table 2). The $\delta^{18}O$ in the grey limestone reaches a mean value of −2.32‰ compared with the mean value of −2.17‰ in the grey marls. In both the greenish-yellow marls and the red marls, the mean value of $\delta^{18}O$ is −1.90‰. The analyses carried out in the contact zone between the red limestone and the bleached zones provide very similar mean values of 1.65‰ and 1.66‰, respectively.

The value obtained from a late calcite vein (100% $CaCO_3$) is $\delta^{18}O = -4.02‰$. The $\delta^{13}C$ data exhibit stable values between a minimum of 1.93‰ and a maximum of 2.12‰. The mean value of $\delta^{18}O$ in a single inoceramid shell in grey facies is 0.39‰, whereas the mean value in different inoceramid shells in red facies is 0.12‰. The $\delta^{13}C$ data exhibit stable values with a slight decrease in the red facies (Table 2). The analysis of grey limestones and marls by XRD indicates that the minority mineral phases correspond to quartz, plagioclase, feldspar, micas and clays such as kaolinite and illite and/or smectite. The presence of hematite is recognized in the insoluble concentrate (Fig. 3d). Cathodoluminescence microscopy (CL) was also used to verify the diagenetic zoning undergone in the inoceramid shells (Fig. 7a–d), and elemental maps (Ca, Fe, Mg) made to determine the presence of ferromagnesian clays in the intercrystalline zones

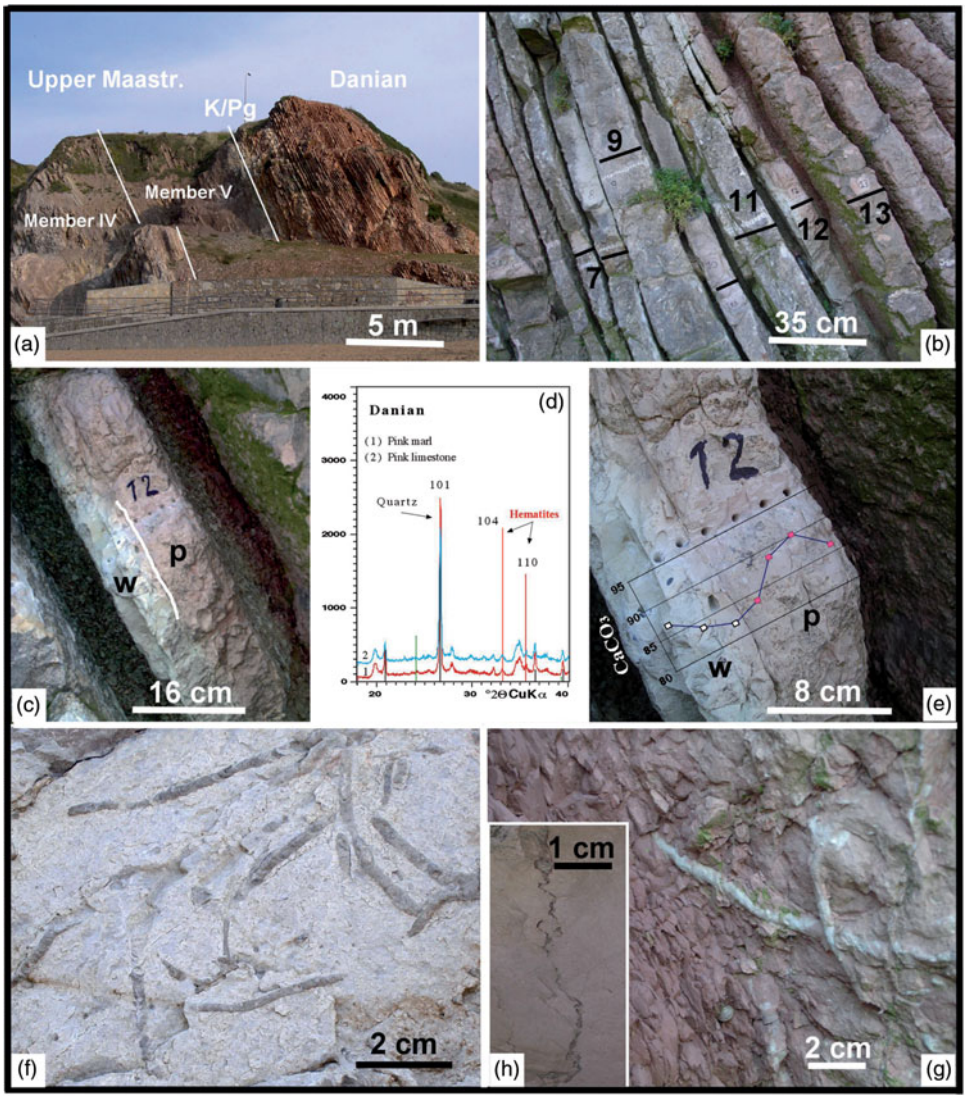

Fig. 6. (Colour online) (a) General view of Member V corresponding to the upper Maastrichtian section, the Cretaceous–Palaeogene border and Danian marl–limestone couplets (Sopelana beach cliffs). (b) View of the Danian pink and white couplets with limestone subcouplets strongly developed versus the marl subcouplets, numbered and sampled for calcimetric analysis. (c) Limestone subcouplet 12, where the clear transition of white (w) to pink (p) limestone is apparent. (d) Diffractograms of the Danian pink marl (1) and pink limestone (2), showing a hematite composition (104 and 110 peaks) in both lithologies. (e) Detail of the 12th couplet with the transition of white limestone at the base to pink limestone with a slight compositional change in the %$CaCO_3$ content. (f) Grey bioturbated marl (*Planolites*), where the non-oxidized traces remain darker in relation to the lower Maastrichtian sediment. (g) In contrast, in the similarly heavily bioturbated pink marls, bleaching occurs in the *Planolites* traces. (h) View of sutured and irregular stylolite with concentration of insoluble material. Examples correspond to (b, c, e, g, h) Danian section and (f) lower Maastrichtian section (Sopelana beach cliff).

of planktonic foraminifer chambers, using an energy-dispersive X-ray spectroscopic instrument (Fig. 8i–l).

5.c. Upper Maastrichtian sections (Sopelana beach cliff)

In Member IV, where inoceramid bivalves are extinct, three small sections were studied (Figs 4a, 5a). Section UM1, of 2.67 m thickness and comprising six marl–limestone couplets with mean values of 20.3 cm thickness for purple marl subcouplets and 17.5 cm thickness for yellowish-grey limestone subcouplets, produces an average sedimentation rate of 2.4 cm ka^{-1}. This UM1 section reveals a greater compositional contrast, with *c.* 20% $CaCO_3$ difference between the purple marl subcouplets ($n = 48$; mean value 48% $CaCO_3$) and the yellowish-grey limestone subcouplets ($n = 83$; mean value 65% $CaCO_3$). Couplets 1, 2 and 3 show greater differences whereas couplets 5 and 6 are more continuous in their composition (Fig. 4a, b; Table 1).

In the same Sopelana cliffs, section UM1 was complemented with another, smaller section, UM1*, with similar lithological characteristics (Fig. 5a). Two complete marl–limestone couplets with a total thickness of 1.39 m were chosen for analysis. These correspond to 53 cm thickness for the two purple marl subcouplets and 86 cm thickness for the two yellowish-grey limestone subcouplets. The average sedimentation rate is 3.5 cm ka^{-1}. The calcimetric analyses of the yellowish-grey limestones ($n = 38$) showed a mean value of 71.5% $CaCO_3$, and of the purple marls ($n = 24$) a mean value of 48.4% $CaCO_3$ (Table 1; Fig. 5a, b, a*). The resulting compositional contrast (> 20%) is similar to that obtained in section UM1.

Section UM2 is 3.60 m in thickness and contains five thicker marl–limestone couplets, with an average thickness of purple marl

Table 1. Mean proportions (%) of $CaCO_3$ and sedimentation rates (cm ka^{-1}) of the marl–limestone couplets analysed in the different selected sections.

Oceanic red beds in the Basque–Cantabrian region	Proportion of $CaCO_3$ (%)	Sedimentation rate (cm ka^{-1})
Muriola beach cliff		
Lower Turonian (Fig. 2d)		
Red marls ($n = 38$)	36.1 ± 5.4	
Grey carbonate turbidites ($n = 23$)	74.6 ± 14.0	
Sopelana beach cliffs		
Lower Maastrichtian section, El Peñón		
Grey limestones ($n = 5$)	78.6 ± 2.6	
Grey marls ($n = 5$)	59.8 ± 2.1	
Greenish-yellow marls ($n = 5$)	61.7 ± 3.2	
Red marls ($n = 5$)	65.3 ± 1.3	
Red limestones ($n = 3$)	86.9 ± 0.6	
Red limestone bleaching ($n = 3$)	90.8 ± 2.5	
Upper Maastrichtian section, UM1 (Fig. 4a)		2.4
Purple marls ($n = 48$)	48.1 ± 9	
Yellowish-grey limestones ($n = 83$)	65.3 ± 5.6	
Upper Maastrichtian section, UM1* (Fig. 5a*)		3.5
Purple marls ($n = 24$)	48.4 ± 7.5	
Yellowish-grey limestones ($n = 38$)	71.5 ± 6.2	
Upper Maastrichtian section, UM2 (Fig. 4a)		3.6
Purple marls (n = 68)	44.7 ± 6.7	
Purple limestones ($n = 82$)	55.4 ± 5.2	
Danian section (Fig. 6b,c,e)		1.2
Pink marls ($n = 11$)	39.4 ± 10	
Pink limestones ($n = 317$)	89.1 ± 4.6	

subcouplets of 38.6 cm and of purple limestone subcouplets of 33.4 cm, with a general detrital contribution noteworthy for its high sedimentation rate (3.6 cm ka^{-1}). The high-resolution calcimetric analysis shows a lower average compositional contrast (*c.* 10%) between the purple marl subcouplets ($n = 68$; mean value 45% $CaCO_3$) and the purple limestone subcouplets ($n = 82$; mean value 55% $CaCO_3$), with a more regular curve visible at couplets 4, 5, 6 and 7. The low $CaCO_3$ contents of the purple limestones indicate that it is more appropriate to define them as marly limestones from now on. The differences between the last values of the marl subcouplets and the first of the marly limestone subcouplets are minimal. Couplet 8 marks a change in this trend (Fig. 3a, c, d; Table 1).

The XRD analysis reveals the presence of hematite in the insoluble concentrate of both purple lithologies. The SEM analysis shows how the carbonate matrix, although cushioned by cementation and compaction, is composed of innumerable coccolith fragments grouped together with illites, such as detrital micas (Fig. 5d, e).

5.d. Danian section (Sopelana beach cliff)

The investigated section, of 3.71 m thickness and comprising 16 continuous marl–limestone couplets, highlights the extreme thinness of the pink marl subcouplets compared with the pink limestone subcouplets (Fig. 6a, b). The average thickness of the limestone subcouplets (19 cm) is much higher on average than that of the marl subcouplets (6.4 cm). The average sedimentation rate is lower (1.2 cm ka^{-1}) than the average value for the Maastrichtian sections discussed above. In the high-resolution calcimetric analysis (*c.* 1 cm per sample) of the marl–limestone couplets, high calcium carbonate contents are observed for the pink and some bleached limestone subcouplets ($n = 317$; mean value of 89% $CaCO_3$) compared with the low values in the pink marls ($n = 11$; mean value of 39% $CaCO_3$) (Fig. 6e; Table 1). The XRD analysis of the pink limestones and the pink marls confirms the presence of hematite in both lithologies in the insoluble concentrate (Fig. 6d). In order to obtain elemental maps (Ca, Fe, Mg) and determine the presence of ferromagnesian clays in the intercrystalline zones, an energy-dispersive X-ray spectroscopic instrument was used (Fig. 8a–h). The SEM analysis shows how the carbonate matrix, although distorted by cementation and compaction, is composed of innumerable coccolith fragments with evidence of bacterial activity (Fig. 9e–h).

6. Discussion

The International Geoscience Programmes 463, 494 and 555 (2002–2010) allowed a substantial advance in our knowledge of

Table 2. Proportions of $CaCO_3$ (%) and isotopic values ($\delta^{13}C$ ‰, $\delta^{18}O$ ‰ V-PDB) of grey, green-yellowish, red (marl–limestone) couplets and bleached parts of El Peñón section, as well as the isotopic values ($\delta^{13}C$ ‰, $\delta^{18}O$ ‰ V-PDB) of the inoceramid prisms collected in the grey and red facies. The isotope data are expressed in the standard δ-notation relative to the Vienna PDB standard (V-PDB). PG – Peñón grey; PV – Peñón greenish-yellow; PR – Peñón red; Pcc – Peñón calcite; SD – standard deviation.

Oceanic red beds in the Basque–Cantabrian region	Limestone	Marl	$CaCO_3$ (%)	Avg	SD	$\delta^{13}C$ (‰)	SD	$\delta^{18}O$ (‰)	SD
Lower Maastrichtian El Peñón section; inverted grey section with thicker inoceramids									
PG-1 (older)	×		81.3			1.94	0.01	−2.32	0.01
PG-2	×		79.9			1.91	0.01	−2.40	0.01
PG-3	×		79.4			1.93	0.01	−2.25	0.02
PG-4	×		74.5			1.93	0.02	−2.31	0.02
PG-5	×		77.8			1.91	0.01	−2.33	0.02
Mean value				**78.6**	**2.6**	**1.93**		**−2.32**	
PG-6		×	62.9			1.95	0.01	−1.92	0.01
PG-7		×	57.5			2.07	0.01	−2.20	0.01
PG-8		×	60.2			2.09	0.01	−2.39	0.02
PG-9		×	60.2			2.07	0.02	−2.21	0.02
PG-10 (younger)		×	58.1			2.12	0.01	−2.15	0.02
Mean value				**59.8**	**2.1**	**2.06**		**−2.17**	
Lower Maastrichtian; greenish-yellow									
PV-1(older)		×	65			2.14	0.02	−1.85	0.02
PV-2		×	65			2.11	0.01	−1.86	0.01
PV-3		×	57.8			2.09	0.02	−1.92	0.02
PV-4 (XRD)		×	60.4			2.12	0.01	−2.13	0.01
PV-5 (XRD)		×	60.2			2.09	0.02	−1.74	0.02
Mean value				**61.7**	**3.2**	**2.11**		**−1.90**	
Lower Maastrichtian (red)									
PR-1		×	63.7			2.10	0.01	−2.11	0.02
PR-2		×	64.8			2.09	0.02	−1.82	0.02
PR-3		×	64.9			2.14	0.01	−1.82	0.02
PR-4 (XRD)		×	66.4			2.11	0.02	−1.85	0.02
PR-5 (XRD) (younger)		×	66.9			2.14	0.02	−1.90	0.02
Mean value				**65.3**	**1.3**	**2.12**		**−1.90**	
Lower Maastrichtian bleached (PRO)									
PRO-1 (Red)	×		87.1			2.05	0.02	−1.61	0.02
PRO-2 (XRD) (Red)	×		86.3			2.05	0.03	−1.65	0.03
PRO-3 (XRD) (Red)	×		87.4			2.03	0.02	−1.70	0.03
Mean value				**86.9**	**0.6**	**2.04**		**−1.65**	
PRO-4 (bleached)	×		88.1			2.05	0.01	−1.58	0.01
PRO-5 (XRD) (bleached)	×		92.2			2.03	0.02	−1.72	0.02
PRO-6 (XRD) (bleached)	×		92			2.05	0.01	−1.70	0.01
Mean value				**90.8**	**2.5**	**2.04**		**−1.66**	
White calcite in fractures									
Pcc-1			100.4			2.04	0.01	−4.02	0.01

(*Continued*)

Table 2. (*Continued*)

Oceanic red beds in the Basque–Cantabrian region	Limestone	Marl	$CaCO_3$ (%)	Avg	SD	$\delta^{13}C$ (‰)	SD	$\delta^{18}O$ (‰)	SD
Inoceramid in grey facies (different fragments from the same shell)									
PE-ino1 shell powder	×					1.84	0.02	0.54	0.02
PE-ino2 shell powder	×					1.86	0.01	−0.45	0.01
PE-ino3 shell powder	×					1.90	0.02	0.02	0.02
PE-ino4 shell powder	×					1.84	0.02	0.52	0.02
PE-ino5 shell powder	×					1.90	0.01	0.33	0.03
PE-ino6 shell powder	×					1.93	0.01	−0.62	0.03
PE-ino1/single prism	×					1.92	0.02	0.96	0.02
PE-ino2/single prism	×					1.75	0.01	0.75	0.01
PE-ino3/single prism	×					1.90	0.02	1.14	0.02
PE-ino4/single prism	×					1.76	0.05	−0.04	0.05
PE-ino5/single prism	×					1.76	0.01	1.09	0.02
Mean value						**1.85**		**0.39**	
Inoceramid in red facies (different specimens)									
PR-INO 1/single prism	×					1.76	0.01	0.60	0.01
PR-INO 2/single prism	×					1.63	0.02	−0.40	0.02
PR-INO 2/single prism/redone	×					1.80	0.01	−0.18	0.01
PR-Ino 3/single prism	×					1.35	0.01	0.18	0.01
PR-INO 3/single prism/redone	×					1.27	0.01	0.22	0.01
PR-Ino 4/single prism	×					1.43	0.02	0.33	0.02
Mean value						**1.54**		**0.12**	

Cretaceous ORBs, including specific studies on chronostratigraphy, sedimentology, mineralogy, elemental and isotopic geochemistry, as well as establishing possible palaeoclimatic and palaeoceanographic relationships between OAEs and Cretaceous ORBs (e.g. Hu *et al.* 2005; Wagreich & Krenmayr, 2005; Wang *et al.* 2005; Chen *et al.* 2007; Cai *et al.* 2009). These investigations were published as SEPM Special Publication no. 91 (Hu *et al.* 2009) and later summarized by Hu *et al.* (2012). Subsequently, this research was expanded upon by other works (e.g. Gambacorta *et al.* 2016; Ahmed *et al.* 2017; Song *et al.* 2017). In summary, the sedimentological, mineralogical and geochemical data suggest that the ORBs were deposited in oligotrophic conditions of cold, oxygenated waters with a low sedimentation rate (Wang *et al.* 2011). The presence of minerals such as nano-grains of ferric minerals that were later all transformed into hematite, goethite and calcite containing Mn^{2+} during early diagenesis is the cause of the homogeneous pigmentation of the red beds (Eren & Kadir, 1999; Wang *et al.* 2009; Cai *et al.* 2012; Hu *et al.* 2012).

However, other investigations suggest additional mechanisms capable of producing red stains in the carbonate materials. Specifically, in the Pennsylvanian red intervals across a well-exposed carbonate slope (Sierra del Cuera, Asturias, NW Spain), the red staining is considered to be the result of iron oxidation that occurred during early diagenesis, taking place within the upper decimetres to metres of the sediment column and driven by suboxic porewaters. This likely involved iron-oxidizing bacteria, while the iron source is attributed to continental influx (Van der Kooij *et al.* 2007). Van der Kooij *et al.* (2007, table 1 and fig. 1) compare different locations in Europe and Australia from early Cambrian to Cretaceous in age, with varied carbonate lithologies and depositional environments such as continental shelf, distal carbonate ramp and deepwater basin, noting possible staining mechanisms such as bacterially mediated oxidation (Della Porta *et al.* 2003; Mamet & Préat, 2006).

Along these same lines, the petrographic and sedimentological study of the Rosso Ammonitico Veronese (Middle–Upper Jurassic, NE Italy) is complemented using classic microscopy, cathodoluminescence and SEM techniques (Préat *et al.* 2006). These authors consider that the red colour is due to bacterially mediated precipitation of iron oxyhydroxides at the water–sediment interface, but under dysoxic–anoxic conditions. Subsequently, these oxyhydroxides were completely transformed into hematite during diagenesis (neomorphism and recrystallization), producing a homogeneous red matrix. Although not mentioned by the authors, it is interesting to verify that, in the few $\delta^{18}O$ values provided (Préat *et al.* 2006, table 1, Voltascura and Forte Campo di Lucerna sections), it can be observed how, in spite of the subsequent diagenesis undergone, the mean values of the red materials are slightly higher ($\delta^{18}O = -0.67‰$; $-0.82‰$) than the mean values of the pink ($\delta^{18}O = -1.17‰$; $-0.98‰$) or grey carbonate matrix ($\delta^{18}O = -1.88‰$; $-1.05‰$). In our opinion, this indicates that the isotopic signal has been partially maintained and that the

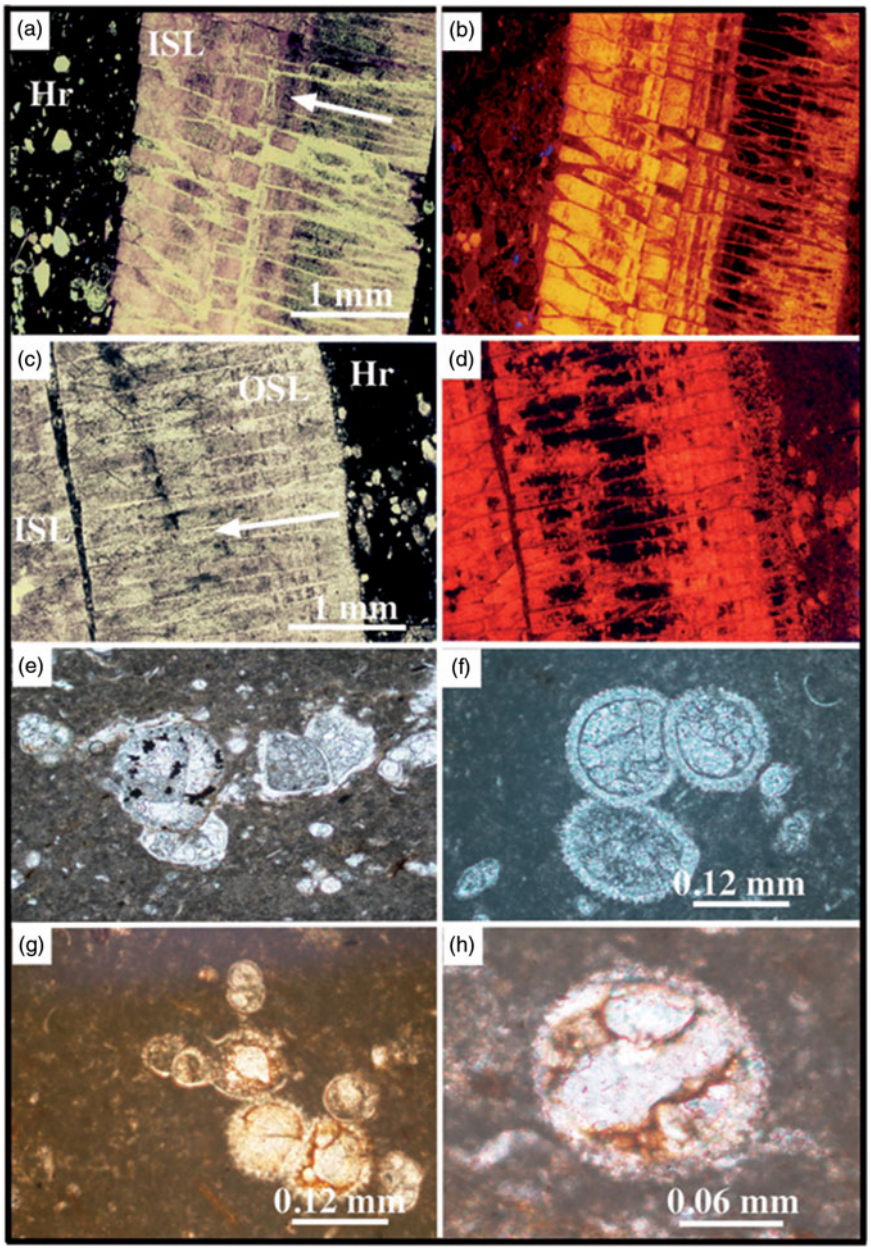

Fig. 7. (Colour online) (a, c) Thin-section views of the inoceramid prismatic microstructure in grey limestone of the lower Maastrichtian section (crossed nicols). (b, d) The same sections under CL, where it is seen how they are partially affected by diagenesis with luminescence in yellow and reddish colours; the central part remains unaltered and non-luminescent. The prisms grow downwards from the outer shell layer (OSL) to the inner shell layer (ISL), as indicated by the white arrows. The host rock (Hr) consists of a mudstone with foraminifer shells and bioclasts. (e) Thin-section view of a grey limestone from the Maastrichtian section (Member II) with planktonic foraminifers, where part of the chambers is infilled by framboidal pyrite crystals (parallel nicols). (f) Thin-section view of the Danian white limestone where the opaque ore surrounds the equant sparry calcite crystals in the chambers. (g, h) Thin-section views of the Danian pink limestone where the calcite fillings of the globigerinid chambers are surrounded by ferromagnesian clays/iron oxides (parallel nicols).

red facies were generated in association with cooler temperatures, gradually becoming warmer in the grey facies.

6.a Collected evidence

6.a.1. Lower Turonian section

This red marl event includes 11 thin grey carbonate turbidites (2–5 cm) with bleaching in the red marls both towards the top and the bottom of the calcarenite turbiditic beds (Fig. 2a–d). The preservation of the turbidite's grey colour is accounted for by an almost instantaneous sedimentation, which prevented oxidation of its components during rapid deposition. However, the turbidites may contain enough organic matter to decompose in the oxidizing environment once deposited. The result is a limited reducing zone that solubilizes and leaches the Fe^{3+} iron oxyhydroxides already present in the red marls until they are bleached, just in the area of influence of the reducing environment. The marl bleaching is more powerful in contact with the bottom than in the turbidite top. If the red colour had occurred during burial diagenesis, once sedimentation was over it would have coloured the marls the same as the carbonate turbidite beds in an ongoing homogenizing process. This bleaching effect in reddish sections due to the

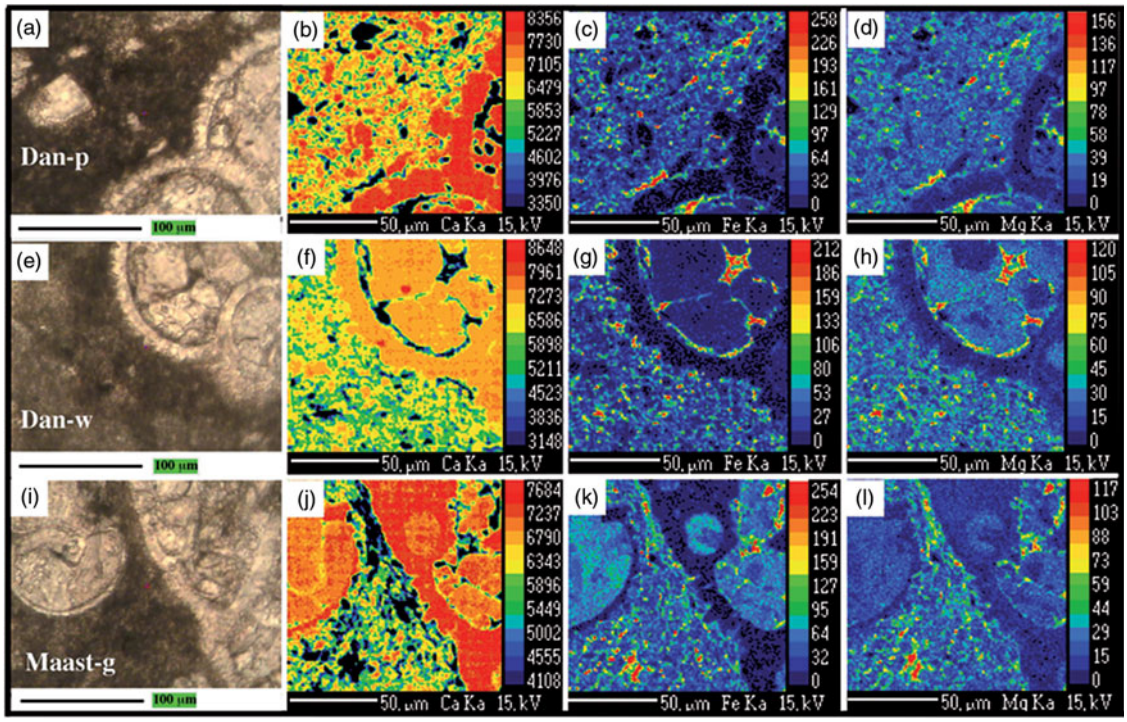

Fig. 8. (Colour online) (a–i) Elemental maps (Ca, Fe, Mg) using an energy-dispersive X-ray spectroscopic instrument, made in three thin-sections belonging to the (a–d) Danian pink (Dan-p), (e–h) Danian white (Dan-w) and (i–l) lower Maastrichtian grey (Maast-g) lithologies. The presence of Ca is predominant in the sections of the foraminifers and in the sparitic cement that fills the chambers. The other elements (Fe, Mg) are arranged in the intercrystalline areas with a higher concentration, indicative of the presence of illite–smectite–chlorite clays, in both the grey-white and pink lithologies. There are areas where the Fe content is predominant, and these regions are interpreted as being where the oxyhydroxides were initially concentrated (now hematite in Dan-p).

presence of turbidite beds seems to be common in many European sections, and has been reported in graph form by different authors (Jansa & Hu, 2009, fig. 1D, p. 61; Wagreich *et al.* 2009; fig. 5C, p. 77; Skupien *et al.* 2009, fig. 8A, p. 108), although its significance has not been explained in depth.

6.a.2. Lower Maastricht

If we assume a constant rate of sedimentation and similar thickness for the marl–limestone couplets, the colour difference must be due to higher oxygen content in the bottom waters and, therefore, a drop in the $Fe^{2+}/(Fe^{2+}+Fe^{3+})$ ratio. It is generally accepted that, for greenish-yellow facies, the ratio for $Fe^{2+}/(Fe^{2+}+Fe^{3+})$ could be higher than 0.5, whereas for red facies the Fe^{2+} has almost completely altered to Fe^{3+}, with a ratio of *c.* 0–0.3 (see Stow, 2005, p. 121).

Epibenthic fauna are affected by the oligotrophic conditions and highly oxic palaeoenvironment, suggested by the scarce presence of small, thin inoceramid shell fragments (thickness < 1 mm) compared with the large (> 20 cm) and thick (6 mm) inoceramids below in the less oxygenated grey facies (Fig. 3b, b*). This interpretation suggests that the oxidizing and cold-water conditions on the seafloor limited the development of such organisms.

On the other hand, evidence of a very early decomposition of organic matter is denoted by both mottled burrows (Fig. 3e) and *Zoophycos* tracings (Fig. 3f), as well as by the scant echinoid macrofossils recognized (Fig. 3g). The early decomposition causes visible bleaching in the limited red area affected. We deduce that the destruction *in situ* of the organic matter, from a living organism, produced a bleached spot (in the sense defined by Tyrell, 1926 and collected in the Glossary of Geology, American Geological Institute). Such a reducing microenvironment is capable of leaching ferric iron and generating hydrogen sulphide, which very occasionally produces small framboidal pyrite crystals (FeS_2). In addition, subsequent brittle fractures in the marl–limestone couplets of the red facies are of note since reducing fluids circulate and cause bleaching unevenly within the zone of influence of the fractures (Fig. 3h); in contrast, although fracturing is present in the grey facies, it is not marked by a change in colour.

A comparison of the isotope values in the grey, greenish-yellow and red materials, as well as in the inoceramid prisms in the El Peñón section, reveal that the red and greenish-yellow materials have higher $\delta^{18}O$ values (mean value $\delta^{18}O = -1.90‰$) compared with the lighter-grey materials (mean value $\delta^{18}O = -2.25‰$). All these values indicate that the trend of the palaeoenvironmental signal (cooler in the red facies than in the grey facies; Wang *et al.* 2011) continues, although modified by burial diagenesis. With respect to the values of the grey facies inoceramids, there is an opposite trend since these values are higher (mean value $\delta^{18}O = 0.38‰$) than those in the red facies (mean value $\delta^{18}O = 0.12‰$). This difference can be explained by the scant thickness (< 1 mm) of the red facies inoceramids, which have been completely affected by diagenesis; in contrast, in the grey facies inoceramids (6 mm thick), the central parts have remained less affected and the average isotope signal is therefore higher (Table 1, Fig. 7a–d).

It is worth noting that the record of the boreal inoceramid *Spyridoceramus tegulatus* (Hagenow, 1842), which coincides with the positive $\delta^{18}O$ excursion, suggests the entry of deep, cold, oxygenated waters from the North Atlantic. These observations confirm the modification of the thermocline and the distribution of

oxygen content in the ocean water column and the onset of climatic cooling around the time of the early–late Maastrichtian boundary, which might have been one of the main causes of the disappearance of inoceramids in the Basque Arc Domain (Gómez-Alday *et al.* 2004).

6.a.3. Upper Maastrichtian

The abrupt colour change from the grey Member II to the purple Member III in the transition from the lower to the upper Maastrichtian section (Fig. 4a) is a good example of palaeoceanographic changes occurring quickly in the shift from a highstand systems tract (HST) (Member II, grey facies, biozone *G. gansseri*) to a lowstand systems tract (LST) (Member III, red facies, biozone *A. mayaroensis*) (MacLeod, 1994; Pujalte *et al.* 2000; Gómez-Alday *et al.* 2004).

Already in Member IV, on the scale of the couplet, when passing from yellowish-grey limestone to purple marl in the marl–limestone couplets, there is a clear, abrupt change (Figs 4a, b, 5a, b). The compositional similarity revealed by XRD (except for the presence of hematite) between the yellowish-grey limestone and purple marl (section UM1) and purple marly limestone and purple marl (section UM2) (Fig. 4a) suggests the same origin of the deposit and that the change in colour occurs during the sedimentation of fundamentally calcareous ooze (coccolithophorids, planktonic foraminifera and ferromagnesian clay remains such as illite and smectite) from the warm surface waters during the Cretaceous greenhouse climate. Recall that the main original components of the limestones, as observed by SEM, are coccolithophorids and detrital clays (Fig. 5d, e) and, in oxygenated and cooler waters with higher viscosity, the sedimentation rate slows down (Stokes' Law); this is why it can more effectively allow the transition from Fe^{2+} to Fe^{3+}. Subsequent burial diagenesis causes the coccoliths, formed of individual plates of calcium carbonate, to partially dissolve, creating micritic cement crystals that bind them together to form the mudstone–wackestone observed in the marl–limestone couplets.

In section UM2, the range of average $\%CaCO_3$ values between the purple marl and the purple marly limestone is significantly small (10%) and sedimentation rates are high (3.6 cm ka^{-1}). These mean values do not coincide with the idea advocated for the Cretaceous ORBs as probably being characterized by a low sedimentation rate (e.g. Hu *et al.* 2012). These marked differences between compositional contrast and average sedimentation rate likely reflect a change from more drastic palaeoenvironmental conditions (rainy versus longer dry periods) to a predominance of wet rainy periods, with increased terrigenous material input and less seasonality (Einsele, 1982; Arthur *et al.* 1984; Einsele *et al.* 1991; MacLeod *et al.* 2001; Giorgioni *et al.* 2012; Jiménez Berrocoso *et al.* 2013).

The purple colour, without reaching red tones, can be well accounted for by: (1) a higher sedimentation rate that does not allow a complete oxidation to red tones during settling to the bottom, despite a high oxygen content of the water mass; or (2) on the contrary, the presence of less oxygenated and more temperate waters, unable to completely oxidize the Fe^{2+} during sedimentation, resulting in purple marl–limestone couplets with $Fe^{2+}/(Fe^{2+}+Fe^{3+})$ values of 0.3–0.5 (Stow, 2005).

6.a.4. Danian section

The palaeogeographic reconstruction of the western Pyrenean area during the Maastrichtian–Paleocene and stratigraphic profiles made by certain authors (Pujalte *et al.* 2000; Baceta *et al.* 2004) confirm substantial colour differences in materials of the same age but from different environments. During the Danian Age, the shallow limestones that formed on a carbonate platform setting (Lizarraga section, Navarra) and the breccias and turbidites that formed on a carbonate slope-apron (section of Aixola, Ermua, Gipuzkoa) are therefore all greyish-white. In contrast, the limestones and hemipelagic marls corresponding to a deep-marine basin setting (Zumaya section, lateral equivalent to the Sopelana section) have the characteristic pink colours (Fig. 1c). This suggests that the triggering factor for pink colouring is likely in the palaeoenvironmental conditions that dominate the basin bottom (cold, oxygenated waters), which do not occur in shallower environments of the same age (carbonate platform and slope-apron), despite having also undergone appreciable diagenetic compaction and recrystallization.

Other evidence on the partial preservation of the palaeoenvironmental signal in the marl–limestone couplets of the Sopelana sections is confirmed by examining the isotopic oxygen values of the lower Maastrichtian and Danian couplets obtained by Jiménez Berrocoso *et al.* (2013). The lower Maastrichtian grey marls have a mean value of $\delta^{18}O = -3.15‰$ ($n = 27$) versus limestones $\delta^{18}O = -3.46‰$ ($n = 42$), whereas the Danian pink marls have an average value of $\delta^{18}O = -1.97‰$ ($n = 22$) and the pink limestones an average of $\delta^{18}O = -2.27‰$ ($n = 28$). These results support the authors' suggestion that, at the level of Milankovitch precession cycles, during the deposition of marls, temperatures were lower (a rainier, colder climate), with a higher detrital contribution from the continent, and with an increase in temperature during the deposition of the calcareous ooze (warmer and drier climate). In turn, the $\delta^{18}O$ average values of the Danian pink marls and limestones are higher (cooler) than in the lower Maastrichtian grey limestones and marls (warmer).

In the Danian section, at the subcouplet scale, it is even detectable how a white limestone bed at the base changes to pink limestone in the middle of the bed, with a clear separation parallel to planar stratification, to continue with a pink marl (Fig. 6a–c, e). Further, a yellowish-grey marl at the base becomes pink towards the top bed and continues with a pink limestone subcouplet, in the image partially covered due to humidity by current green algae (Fig. 6c, e). Strong bioturbation (*Planolites*) recorded in the lower Maastrichtian grey marls and the Danian pink marls also provides an insight into their different settings. In the grey marls, fossil traces remain darker than sediment (Fig. 6f), proof that the environment did not have enough oxidative capacity to break down the organic matter provided by the organism; in contrast, in the pink marls the fossil traces are bleached (Fig. 6g) by substantial organic matter oxidation.

6.b. Burial diagenesis and partial preservation of the palaeoenvironmental signal

In thick Cretaceous and Paleocene sedimentary series, such as those produced in the Basque–Cantabrian Basin, there is no doubt that early and burial diagenesis occurred with different degrees of intensity, according to the height of the selected column as well as its location with respect to the depocentre or the lateral zones of the basin (Arostegui *et al.* 1991, 2006; Ortega-Huertas *et al.* 1995; Sangüesa *et al.* 2000). Published works on the diagenetic activity in the marl–limestone grey couplets of the lower Maastrichtian section demonstrate their effects by variations in luminescence and isotopic changes that are determined both in thick-shelled epibenthic inoceramid organisms as well as in the grey marl–limestone couplets themselves. Illite is the most abundant clay mineral (< 2 μm), reaching a mean value of about 58%, followed

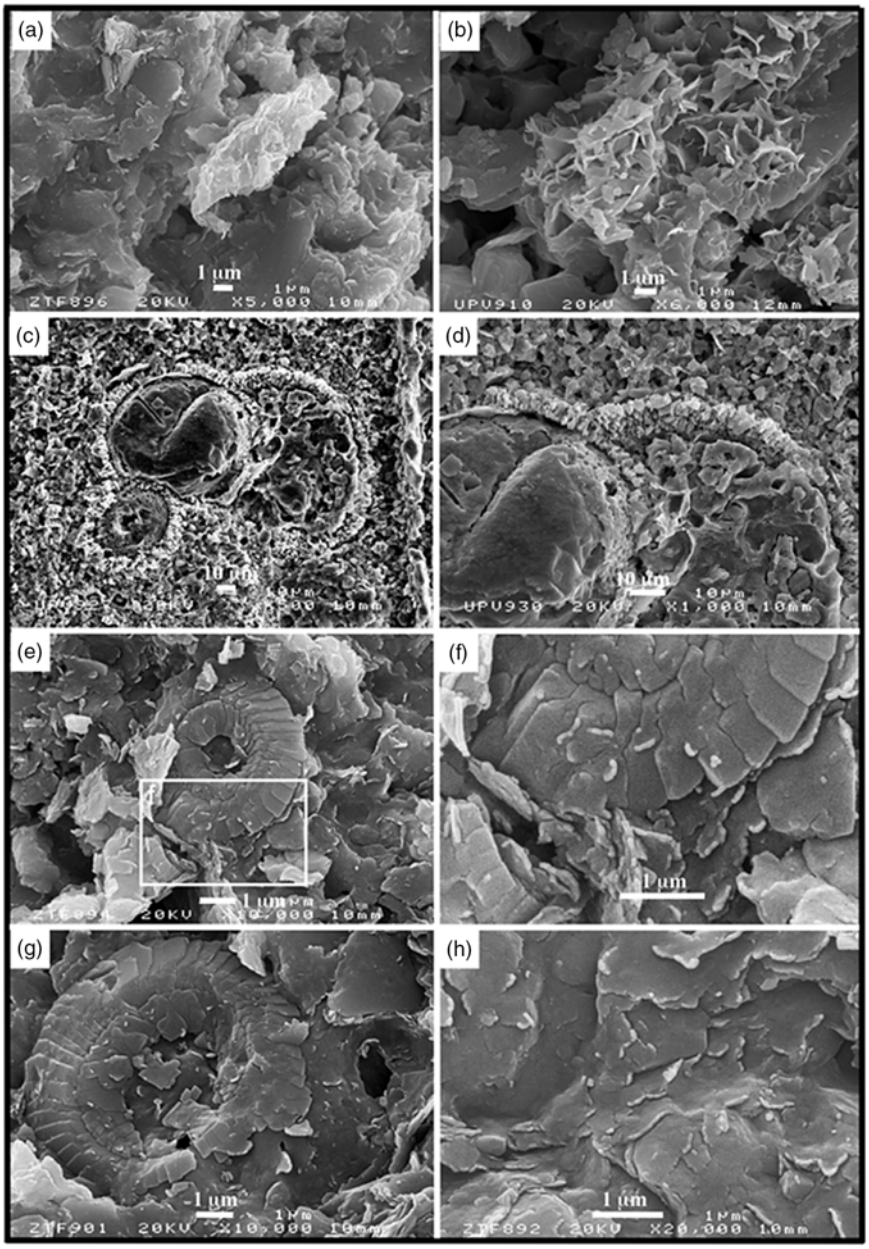

Fig. 9. SEM images of whole-rock samples. (a, b) Larger detrital mica in the process of diagenetic alteration and an aggregate of illite–smectite (I-S) mixed layer (R1) in the calcareous ooze from the Danian section. (c, d) General appearance and detail of the chambers of a planktonic foraminifer filled by sparry cement. (e, h) Views and details of the calcareous ooze formed by coccolith plates and ferromagnesian clays, with evidence of nanobacterial activity in both.

by chlorite (13%) and kaolinite (11%). The illite–smectite (I-S) mixed layers (R1, 17% illite) and $\delta^{18}O$ (−2.89‰ PDB) also indicate diagenetic alteration (Fig. 9a, b) (Gómez-Alday *et al.* 2008).

These same trends of diagenetic alteration in inoceramids and deep-marine sediments are also detected in grey materials from the Coniacian–Santonian sections of the Basque–Cantabrian Basin. The transformations of the clay minerals have been recognized with more diagenetically advanced illite–smectite (I-S) mixed layers (R1, 70% illite), authigenic chlorite and low $\delta^{18}O$ (−4.05‰ PDB) in the Barrika section (deep-marine basin) versus the platform-marine (Isla de Castro, Villamartín and Olazagutía) settings (Fig. 1a, c). All these transformations are good indicators of the diagenetic activity undergone by these sediments, which reached burial depths of up to 6–9 km (Jiménez Berrocoso *et al.* 2004, 2008).

However, despite having undergone greater or lesser degrees of diagenetic alteration, the palaeoenvironmental signal can still be detected, preserved in inoceramid shells under CL (Fig. 7a–d), oxygen isotopes, mean $^{87}Sr/^{86}Sr$ isotope ratios (0.707819 ± 0.000003 (2σ, $n = 8$) and also in the sediments, although in more attenuated form, in very favourable conditions (Gómez-Alday *et al.* 2004, 2008). The vertical distribution and variability of the clay minerals (< 2 μm) observed is therefore not likely to be the exclusive product of their diagenetic transformation; at 25–40 m, the sediment thickness is not enough to record notable changes in diagenetic gradients between the bottom and the top of the recognized

stratigraphic sections. Instead, tectonosedimentary causes related to unsuitable conditions for clay formation and transport from the local source areas contributed to the original clay differences (Jiménez Berrocoso *et al.* 2008). Finally, Jiménez Berrocoso *et al.* (2013) considered that the fine-scale (2 cm per sample) geochemical and sedimentological (%$CaCO_3$, $\delta^{18}O$ and $\delta^{13}C$) records of calcareous couplets challenge purely diagenetic explanations. The lower Maastrichtian transition to a transgressive system tract therefore favoured a greater influence of oceanic processes in the depositional setting, whereas a relatively cool, oxygen-rich water mass with high oxidation potential influenced the geochemical and depositional patterns of Danian couplets. In other words, the geochemical and sedimentological patterns of these calcareous couplets were caused by the interplay of climate, palaeogeography and oceanography as forcing mechanisms.

6.c. End-Cretaceous North Atlantic Ocean circulation

To explain the cooling detected by the oxygen isotope signal during the early Maastrichtian Age and the presence of the boreal inoceramid *Spyridoceramus tegulatus*, Gómez-Alday *et al.* (2004) suggest that there is a change in the type of thermohaline circulation due to the entry of deep, cold waters from high latitudes that results in greater temperature stratification in the oceans. Apparently, the origin of these deep, cold waters varied throughout the Maastrichtian Age. Up to the lower–upper Maastrichtian boundary, the ocean floor was occupied by saline and warm oxygen-poor waters with an origin in the vast epicontinental seas of the globe. During this boundary period, deep, cold and dense waters formed in the polar regions and reached low latitudes to form the intermediate and deep waters of the tropics (Saltzman *et al.* 1982; Barron *et al.* 1984; MacLeod *et al.* 2011; Huber *et al.* 2018). Further, Gambacorta *et al.* (2016) defend the same idea: "... although the paleotemperature reconstructions are still loose, reddish lithologies corresponding to times of relatively cooler conditions might indicate a mechanism of deep water formation different from saline waters at low-latitude characteristic of warm climatic conditions. Possibly, during times of decreasing temperature after warming episodes, cooler oxygen richer bottom water masses originated at higher latitudes."

6.d. Iron source and distribution of Fe^{3+} in the sediment

Riverine, atmospheric, iceberg, hydrothermal and diagenetic recycling are thought to be the main iron (Fe) sources in oceans (Raiswell & Canfield, 2012). Iron in the environment exists in two redox states: Fe^{2+} and Fe^{3+}. The abundance of each iron form depends on the pH/Eh conditions in which the Fe species are thermodynamically more stable. Through enzymatic activity, bacteria can catalyse redox reactions. In the oceans, dissolved Fe concentrations can be as low as 0.02–2 nM in oxygenated waters and as high as 300–3000 nM in anoxic waters (De Baar & De Jong, 2001). Gledhill & Buck (2012) point out that about 99.9% of dissolved Fe^{3+} in seawater is bound to organic molecules as Fe-binding ligands (FeL); the mean maximum FeL concentration can reach *c.* 4 nM. The existence of FeL explains why Fe^{3+} is retained in solution instead of forming iron (oxyhydroxide) precipitates. Dissolved Fe^{2+} appears at very low concentrations in oxic seawater due to rapid oxidation by its two main oxidants, oxygen (O_2) and hydrogen peroxide (H_2O_2). Organic ligands can also stabilize Fe^{2+}, which may circumvent the rapid transformation to oxyhydroxides (Breitbarth *et al.* 2010). Consequently, Fe^{2+} and Fe^{3+} can be either inorganic or complexed to dissolved organic compounds.

Biogenic iron concentrations in surface waters constitute an important pool of Fe since this element is a limiting nutrient for phytoplankton. Inorganic Fe^{3+} is more available for biota than organic Fe-bearing complexes, but primary producers establish mechanisms for taking up aqueous Fe^{3+} species as well as solubilizing iron (oxyhydroxides). The transformation of organic matter to simpler dissolved organic compounds during sinking may play a role in the speciation and complexation of Fe^{2+}. Under oxygen-deficient conditions, as described by Heller *et al.* (2017) in modern ocean oxygen-minimum zones, the regeneration of Fe^{2+} contained in organic matter can be coupled to microbially mediated nitrate (NO_3^-) and reduction to nitrite (NO_2^-). Fe^{3+} formation, and the subsequent hydrolysis and precipitation of oxyhydroxides, may therefore take place within the water column. Fe contained in Fe-bearing minerals can be released through diffusive outflow from sediment pore water to the water column (Raiswell & Canfield, 2012). For instance, Fe can be carried by clay minerals, either as part of the clay structure or, highly important, as oxide films on the surface of clays (Tucker, 1994). The microbial reduction of iron oxyhydroxides during the decomposition of organic matter (Noffke *et al.* 2012), for example, produces dissolved Fe^{2+} in high concentrations in oxygen-depleted marine sediments. If the overlying water contains oxygen, reduced Fe^{2+} is oxidized by O_2 or H_2O_2 to Fe^{3+}, which forms oxyhydroxide precipitates.

In our case, traditional microscopy reveals that the iron forms aggregates of framboidal pyrite on the edges of the microsparite crystals that fill the chambers of the foraminifers encased in the grey limestones of the lower Maastrichtian (Fig. 7e). However, such pyrite formations do not occur in the Danian white limestones (Fig. 7f). In contrast, it can be seen how, in the filling of the foraminifer chambers of the Danian pink limestone, the microsparite cyrstals are covered by iron oxides/ferromagnesian clays (Figs 7g, h, 9c, d). This difference seems to indicate the lack of incorporation of the iron into the microstructure of the microsparite–sparite as a product of the neoformation–diagenetic recrystallization.

The elemental maps (Ca, Fe, Mg) were examined using an energy-dispersive X-ray spectroscopic instrument on three thin-sections belonging to the Danian pink and white (Dan-p; Dan-w) and Maastrichtian lower grey (Maast-g); the examination reveals that Ca is the dominant element in the foraminifer sections and in the sparitic cement that fills the chambers. The other elements (Fe, Mg) are arranged in the intercrystalline areas with a higher concentration, indicative of the presence of ferromagnesian clays (illite–smectite–chlorite) in both the grey-white and pink lithologies. There are areas where Fe predominates and can be interpreted as belonging to oxyhydroxides (later hematite in Dan-p); or (later pyrite in Dan-w/Maast-g) although, because of the size of the possible crystals (< 10 nm) found by Cai *et al.* (2012) in Vispi Quarry limestones, the resolution of our image does not allow us to directly observe the crystals (Fig. 8).

Bacterial activity was certainly a factor in the development of the pink colour of the Danian couplets (Fig. 9e–h); however, in the absence of more precise studies, it cannot be considered the primary cause of the red colouring in the case of the Basque–Cantabrian Basin, even though other authors consider iron-oxidizing bacteria to be the main cause of such tones in their studies on other areas (Mamet *et al.* 1997; Della Porta *et al.* 2003; Mamet & Préat, 2005, 2006; Préat *et al.* 2006, 2018; Van der Kooij *et al.* 2007; Song *et al.* 2017). Nanobacteria with coalescent structure forms (< 0.1 μm) thrive in the superficial part of the coccolith plates and ferromagnesian clays, with a strong similarity to those reported by Mamet & Préat (2006, fig. 1A), Préat *et al.* (2006, fig. 8C–F).

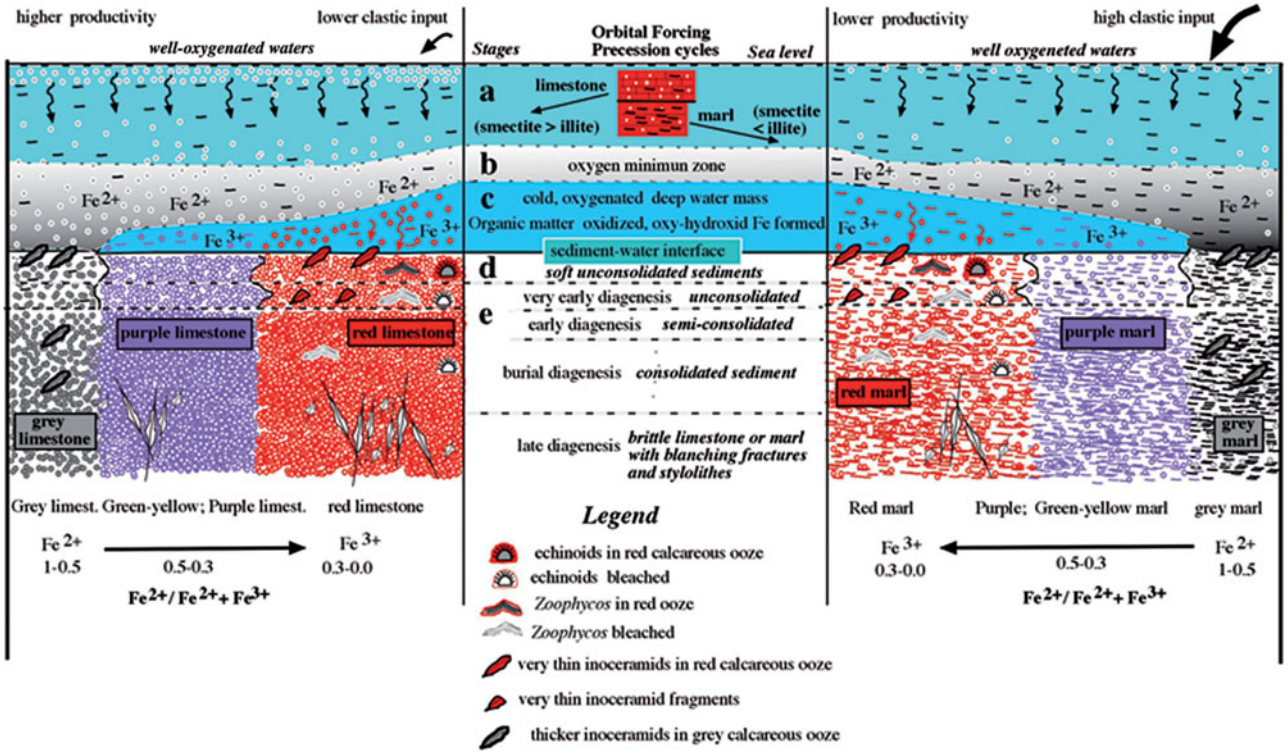

Fig. 10. (Colour online) Deep-facies depositional model for the formation of the marl–limestone couplets belonging to the Maastrichtian and Danian sections at the Sopelana beach cliffs. They depend on the residence time that the foraminifers and coccolith debris and the ferromagnesian clay minerals spent passing, or not, through occasional masses of cold, oxygenated water to reach the sea bottom. The unconsolidated deposits acquire different shades of grey to greenish-yellow, purple, pink and finally red. These colours are generated during synsedimentary deposition and are interpreted as a depositional feature.

As a result of the points discussed above, we discard the notion that reddish-pink to greenish-yellow tones are the main product of early diagenesis, as claimed by other authors (Eren & Kadir, 1999; Hu *et al.* 2005, 2012; Jansa & Hu, 2009) in the Cretaceous ORBs of the Tethysian and North Atlantic basins. We are in favour of a synsedimentary process, where the deposition of the calcareous ooze involved mainly coccolithophorids, planktonic foraminifers and ferromagnesian clays derived from the oceanic surface and continental sources, and was sedimented towards the sea bottom through cold, oxygenated waters. These waters are not only available at different heights of the water column, but can reach the sea bottom and remain for long enough for oxidation to occur (MacLeod *et al.* 2011). The coating of the calcareous particles by oxyhydroxides during the slow sedimentation was conditioned by a lower temperature of the oxidizing waters and the availability of Fe^{2+}. The different red, pink and greenish-yellow colours may be determined by the sedimentation rate and/or oxidation capacity of the water mass. The red colour in the marl–limestone couplets was already present before the organic decomposition of echinoids, and the trace markers of ichnofossils such as *Planolites* and *Zoophycos*, was able to generate a reducing zone, with centimetric extension and bleaching of both the limestones and the marls (Fig. 3e–g). Even the presence of grey carbonate turbidites included in red marls indicates that the process is of synsedimentary origin and did not occur during burial diagenesis (Fig. 2b, c).

We have attempted a simplified model with the differentiated vertical marine stages represented schematically (Fig. 10), as well as possible variations in temperature and oxidation capacity of the water mass, which allows us to distinguish at least five types of couplets according to their variable colouring (Table 3).

6.e. First possibility during sedimentation (stages (a) and (b))

Particles settling until reaching the basin bottom pass through different stages. (a) This stage ranges from the marine surface, where lesser or greater organic seasonal productivity occurs, to the oxygen minimum zone (OMZ), with a part of the organic matter still preserved. A greater or lesser contribution of clastic materials determines the subsequent formation of marls or limestones controlled by processional cycles (Fig. 10). (b) In the transit through the OMZ, with sufficient thickness and an appreciable lack of oxygen and light, partial decomposition of organic matter from protozoans (foraminifers, radiolarians) and algae (coccolithophores) is triggered, and Fe^{2+} is consequently liberated in this reducing zone. Settling continues until the basin bottom, where the residual organic matter is associated with calcareous ooze in a dysoxic environment, but always above the carbonate compensation depth (CCD). The presence of Fe^{2+} as pyrite (FeS_2) precipitation and ferromagnesian clays can be recognized inside microforaminifer chambers (Figs 7e, 8).

As a result, substantial grey sediment formation is arranged in the marl–limestone couplets, governed by orbital precession variations (*c.* 20 ka), consisting mainly of a calcareous ooze component and a larger (marls) or smaller (marly limestone to limestones) concentration of inherited clays (illite–smectite, kaolinite) undergoing alteration with the liberation of cations. The presence of epibenthic organisms such as large inoceramids and ichnofossils such as *Planolites* and *Zoophycos* in both the limestones and marls is remarkable. Subsequently, burial diagenesis generated neomicrite (< 1 μm) that successively underwent recrystallization to larger particles such as micrite (< 4 μm) and microsparite (> 4 μm), and the neoformation of illite–smectite (I-S) mixed layers, chlorite and illite agregates

Table 3. Possible conditions (temperature and oxidation capacity) of water mass at the seafloor for the five cases proposed to explain colouring in the marl–limestone couplets.

Case no.	Water mass conditions and causes	Marl–limestone couplet
1	Water mass with high oxidation capacity and sufficient thickness: • conditioned by the settling velocity, sedimentation rate and content in ferromagnesian clay in each subcouplet; • the temperature of the waters is always colder than in grey facies.	Pink marls, pink limestones, red marls, red limestones
2	Water mass with sufficient oxidation capacity, but without achieving complete material oxidation: • high sedimentation rate; depletion capacity of water oxidation with a thickness similar to case 1; • smaller water mass thickness does not give time for complete oxidation due to the high sedimentation rate in marl–limestone couplets; • slight warming of temperature and a higher settling velocity do not allow complete oxidation in the water masses.	Purple marls, purple limestones
3	Water mass with limited oxidation capacity, without achieving complete oxidation: • low quantity of detritic clays bearing Fe during settling and formation of limestone subcouplet; • higher settling velocity of the carbonate particles of the limestone subcouplet compared with the majority clays of the marl subcouplet; • independent of the temperature and thickness of the water masses.	Purple marls, yellowish-grey limestones
4	Rapid change in the oxidation capacity of the water mass towards more oxidizing and cold waters: • the thickness of the water masses can grow and enhance the oxygenation capacity; with this trend, the settling velocity decreases and the sedimentation rate has no decisive influence.	Modification from grey couplets to greenish-yellow to red couplets
5	No oxidation capacity of the water mass: • settling velocity and sedimentation rate similar, with greater temperature of the water masses.	Grey marls, grey limestones

produced the compaction–recrystallization and consequent differentiation of the couplets according to their content in clays and carbonate (Figs 3a, 4a).

6.f. Second possibility during sedimentation (stages (a–c))

Recall that it is accepted in the literature that Cretaceous ORBs were deposited in oligotrophic conditions of cold, oxygenated waters with a low sedimentation rate (Hu *et al.* 2012). In accordance with the evidence presented above, it is therefore also possible that in our basin a mass of denser-than-usual cold, oxygenated waters were incorporated from the North Atlantic Sea, possibly comprising tongues advancing and retreating on the basin bottom at temporary intervals as short-term ORBs (< 1 Ma). Stages (a) and (b) have the same characteristics as those described in Section 6.e above (first possibility), but stage (b) does not reach the sediment–water interface because the transitory arrival of colder, oxygenated water would lead to important changes in the biogeochemical cycles by modifying the extent of the OMZ. (c) The slower settling of ferromagnesian particles (Fig. 9a) and their passage through the mass of cold, well-oxygenated water allows the Fe^{2+} to Fe^{3+} to be transformed into oxyhydroxides. These can occur on the surface and interior of particles (detrital/shells) as a fine film (Tucker, 1994), and are deposited on the sediment–water interface as pigmented calcareous ooze.

The sediment has different colours (red, pink, greenish-yellow) depending on its settling speed and the oxygen content, and therefore the $Fe^{2+}/(Fe^{2+}+Fe^{3+})$ ratio, of the water. It is even possible to determine the appearance of the tongues of cold, oxygenated waters during the initial formation of a white-grey limestone subcouplet that ends up as a pink limestone, with the same morphological characteristics and with a slight increase in the $\%CaCO_3$ contents (Fig. 6c, e).

6.g. Soft, unconsolidated sediments (stage (d))

(d) The calcareous ooze is already pigmented at the water–sediment interface, and a significant number of epibenthic organisms are recorded, such as small, thin inoceramids, echinoids and trace fossils such as *Zoophycos* and *Planolites*. The rapid post-mortem decomposition of organic matter generated a limited reducing environment around these remains, recognizable by bleaching due to the leaching of Fe^{3+} (Fig. 3e–g). It is possible to differentiate between the soft unconsolidated sediments and the next phase of still unconsolidated sediments until very early diagenesis began.

6.h. Very early diagenesis and burial diagenesis (stage (e))

(e) Partial or complete dissolution of the calcareous ooze allowed neomicrite formation (< 1 μm) that successively underwent recrystallization to larger particles such as micrite (< 4 μm) and microsparite (> 4 μm). Under normal microscopy, it seems that ferromagnesian clays and iron oxides (hematite) are not substantially incorporated and do not form part of the neoformed matrix crystals (micrite–microsparite) and that, in the foraminifer chambers, these minerals surround the new sparite cement without incorporating it (Fig. 7g, h). The Fe^{3+} now forming nanocrystals of hematite seems to have been distributed in the matrix, but it does not become part of the sparry calcite in the filling of the foraminifer chambers. This interpretation suggests that the pigmented calcareous ooze pre-dates diagenesis as a dominant depositional feature (Fig. 8). As a result, the marl–limestone coloured couplets (red, pink, greenish-yellow) form according to the $Fe^{2+}/(Fe^{2+}+Fe^{3+})$ ratio.

6.i. Late diagenesis

This stage is evidenced by limited and irregular fracturing of the already consolidated rock with slight displacement that allows the circulation of reducing fluids and the consequent dissolution of Fe^{3+} recognized by the bleaching in the red facies (Fig. 3h). In the greenish-yellow layers, the bleaching is more muted and barely perceptible, but it also occurs in the El Peñón section. Another late-diagenesis characteristic of the Danian limestone subcouplets is the presence of numerous small, sutured and

irregular stylolites perpendicular to the stratification surface. These are caused by a pressure–dissolution effect and are recognized at first sight by the concentration of insoluble material that highlights the suture (Fig. 6h). Analysing this concentrated residue by XRD confirms the presence of ferromagnesian micas, quartz, plagioclase and small amounts of hematite.

7. Conclusions

The ORBs present in Upper Cretaceous and Danian sections in the Basque–Cantabrian Basin are exceptional due to the presence and regularity of their marl–limestone couplets, together with the macroscopic, microscopic and geochemical evidence collected. Five types of marl–limestone couplets can be differentiated according to the exposed colouring: (1) pink-red marl versus pink-red limestone; (2) purple marl versus purple limestone; (3) greyish-yellow limestone versus purple marl; (4) steps from grey to greenish-yellow to red marl–limestone couplets; and (5) grey marl versus grey limestone. The sedimentation rate is variable, but in contrast to what is published on Cretaceous ORBs, it can be high (3.6 cm ka^{-1}) in the coloured couplets. The oxygen isotopic signal in the lower–upper Maastrichtian and Danian sections and the presence of the boreal inoceramid *Spyridoceramus tegulatus* serve to confirm the presence of deep, cold, oxygenated waters surely coming from high latitudes (North Atlantic). The variation in colours is interpreted as the possible palaeoenvironmental transit of the particles, mainly calcareous nannoplankton such as coccolith plates, planktonic foraminifers and detrital clays, which settle slowly in dysoxic environments forming grey marl–limestone couplets. However, as they circulate through a cooler and more oxidizing water body, they change to greenish-yellow, purple and pink until finally reaching red tones based on the $Fe^{2+}/(Fe^{2+}+Fe^{3+})$ ratio. Hematite, considered the main staining agent, was detected by XRD together with the ferromagnesian clays. The colouring is considered a depositional factor, without discarding the possible redistribution of oxyhydroxides changing to hematite as a final product. Given the nanometric size of the hematite particles, they are difficult to detect by SEM-EDX. The shell and chamber filling of the foraminifers do not incorporate appreciable amounts of Fe and Mg during diagenesis. In the intercrystalline sparry cement, ferromagnesian clays are distributed as detected by the Ca, Fe and Mg maps. Fe in grey facies is present as Fe^{2+} (pyrite). Nanobacterial activity is also detected, present both in the coccolith plates and in the ferromagnesian micas, without it being possible to establish its importance in the staining process.

Acknowledgements. JE is supported by the Universidad del País Vasco/Euskal Herriko Unibertsitatea, Spain (UPV/EHU, research group GIU18/16317/05) and by the Elorza Foundation. We thank Dr Ana Pascual (UPV/EHU) for the micropalaeontological determination. We thank the anonymous referees for their comments, which have significantly enriched the contents of the manuscript. We are also grateful to Christine Laurin and Rupert Glasgow for improving the English.

References

Ahmed MJ, Tamar-Agha MY and Alwan TA (2017) Geochemistry and depositional conditions of the Cretaceous oceanic red beds (CORBs) within the Shiranish Formation in North of Iraq. *Iraqui Journal of Science* **58**, 2139–64.

Allison LE and Moodie CD (1965) Carbonate: volumetric calcimeter method. In *Methods of Soil Analysis. Part 2. Chemical and Microbiological Methods* (ed CA Black), pp. 1389. Madison, WI: American Society of Agronomy.

Alonso de Linaje V, Fernández-Lerín B, Apodaca J, Biain A, Jaca E, Hernández-Martín S and Elorza J (2009) Turbiditas carbonatadas en la Playa de Muriola (Barrika, Arco Vasco): edad, deformación, contenidos de $CaCO_3$ y presencia de barita diagenética. *Geogaceta* **47**, 69–72.

Álvarez-Llano I, Baguer A, Martínez López de Sabando M, Múgica J, Pérez-García JR, Unanue L and Elorza J (2006) Variaciones de espesor y de contenido en $CaCO_3$ en los pares marga-caliza del Maastrichtiense inferior en Sopelana (Arco Vasco). *Geogaceta* **39**, 131–4.

Arenillas I, Arz JA and Molina E (1998) El límite Cretácico-Terciario en Zumaya, Osinaga y Músquiz (Pirineos): control bioestratigráfico y cuantitativo de hiatos con foraminíferos planctónicos. *Revista de la Sociedad Geológica de España* **11**, 127–38.

Arostegui J, Sangüesa FJ, Nieto F and Uriarte JA (2006) Thermal models and clay diagenesis in the Tertiary-Cretaceous sediments of the Alava block (Basque-Cantabrian basin, Spain). *Clay Minerals* **41**, 791–809.

Arostegui J, Zuluaga MC, Velasco F, Ortega-Huertas M and Nieto F (1991) Diagenesis of the Central Basque-Cantabrian basin (Iberian Peninsula) based on illite-smectite distribution. *Clay Mineralogy* **26**, 535–48.

Arthur MA, Brumsack H-J, Jenkyns HC and Schlanger SO (1990) Stratigraphy, geochemistry, and paleoceanography of organic carbon rich Cretaceous sequences. In *Cretaceous Resources Events and Rhythms* (eds R Ginsburg and B Beaudoin), pp. 75–119. Netherlands: Kluwer Academic Press.

Arthur MA, Dean WE, Bottjer DJ and Scholle PA (1984) Rhythmic bedding in Mesozoic–Cenozoic pelagic carbonate sequences: the primary and diagenetic origin of Milankovitch-like cycles. In *Milankovitch and Climate Part I* (eds A Berger, J Imbrie, J Hays, G Kukla and B Saltzman), pp. 191–222. Dordrecht: Riedel.

Baceta J, Pujalte V, Serra-Kiel J, Robador A and Orue-Etxebarria X (2004) El Maastrichtiense final, Paleoceno e Ilerdiense inferior de la Cordillera Pirenaica. In *Geología de España* (ed JA Vera), pp. 308–13. Madrid: SGE-IGME.

Barron EJ, Saltzman E and Price DA (1984) Occurrence of *Inoceramus* in the South Atlantic and oxygen isotopic palaeotemperatures in Hole 530A. In *Initial Reports of the Deep Sea Drilling Project*, no. 75 (eds WW Hay and J-C Sibuet), pp. 893–904. Washington: US Government Printing Office.

Beil S, Kuhnt W, Holbourn A, Scholz F, Oxmann J, Wallmann K, Lorenzen J, Aquit M and Chellai EH (2019) Cretaceous oceanic anoxic events prolonged by phosphorus cycle feedbacks. *Climate of the Past*, published online 8 October 2019, https://doi.org/10.5194/cp-2019-118.

Breitbarth E, Achterberger ET, Ardelan MV, Baker AR, Bucciarelli E, Chever F, Croot PL, Duggan S, Gledhill M, Hasselhov M, Hoffmann LJ, Hunter KA, Huthins DA, Ingri J, Jickells T, Lohan MC, Nielsdottir MC, Sarthou G, Schoemann V, Trapp JM, Turner DR and Ye Y (2010) Iron biogeochemistry across marine systems-progress from the past decade. *Biogeosciences* **7**, 1075–97.

Cai Y, Hu X, Li X and Pan Y (2012) Origin of the red colour in a red limestone from the Vispi Quarry section (central Italy): a high-resolution transmission electron microscopy analysis. *Cretaceous Research* **38**, 97–102.

Cai Y, Li X, Hu X, Chen X and Pan Y (2009) Paleoclimatic approach to the origin of the coloring of Turonian pelagic limestones from the Vispi Quarry section (Cretaceous central, Italy). *Cretaceous Research* **30**, 1205–16.

Chen X, Wang CS, Hu X, Huang Y, Wang P, Jansa L and Zeng X (2007) Global correlation of Cretaceous oceanic red beds. *Acta Geologica Sinica (English Edition)* **81**, 1070–86.

De Baar HJW and De Jong J (2001) The biogeochemistry of iron in seawater. In *Distributions, sources and sinks of iron in seawater* (eds D Turner and K Hunter), pp. 123–253. Chichester, UK: John Wiley & Sons Ltd. IUPAC Series on Analytical and Physical Chemistry of Environmental Systems no. 7.

Della Porta G, Mamet B and Préat A (2003) Microbial mediation in the formation of red limestones, Upper Carboniferous, Cantabrian Mountains, Spain. In *Proceedings of the XVth International Congress on Carboniferous and Permian Stratigraphy* (ed ThE Wong), pp. 10–16. Utrecht: Royal Netherlands Academy of Arts and Sciences.

Dickson JAD (1965) A modified staining technique for carbonates in thin section. *Nature* **205**, 587.

Dinarès-Turell J, Pujalte V, Stoykova K and Elorza J (2013) Detailed correlation and astronomical forcing within the Upper Maastrichtian succession in the Basque Basin. *Boletín Geológico y Minero* **124**, 253–82.

Domínguez E, Echeverría J, Gómez-Urtasun I, Ibisate R, Martínez-García B and Elorza J (2007) Espesores y contenido en $CaCO_3$ en los pares marga-caliza del Daniense (Sopelana, Arco Vasco). *Geogaceta* **41**, 67–70.

Einsele G (1982) Limestone-marl cycles (periodites): diagnosis, significance, causes—a review. In *Cyclic and Event Stratification* (eds G Einsele and A Seilacher), pp. 8–53. New York: Springer-Verlag.

Einsele G, Ricken W and Seilacher A (1991) *Cycles and Events in Stratigraphy*. New York: Springer-Verlag, 955 p.

Elorza J and Bustillo MA (1989) Early and late diagenetic chert in carbonate turbidites of the Senonian flysch, N.E. Bilbao. Spain. In *Siliceous Deposits of the Tethys and Pacific Regions* (eds JR Hein and J Obradovic), pp. 93–105. New York: Springer-Verlag.

Elorza J, Orue-Etxebarria X and Lamolda MA (1984) Existencia de una fracturación intensa en el área de Sopelana-Meñacoz (N.E. Bilbao). In *Actas I Congreso Español de Geología*, vol **III**; pp. 177–84. Madrid: SGE-IGME.

Eren M and Kadir S (1999) Colour origin of upper cretaceous pelagic red sediments within the Eastern Pontides, northeast Turkey. *International Journal Earth Sciences* **88**, 593–5.

Floquet M (2004) El Cretácico Superior de la Cuenca Vasco Cantábrica y áreas adjacentes. In *Geología de España* (ed JA Vera), pp. 299–306. Madrid: SGE-IGME.

Fugger E and Kastner C (1885) *Naturwissenschaftliche Studien und Beobachtungen aus und über Salzburg. Die Steinbrüche von Bergheim und Muntigl*. Salzburg: Hermann Kerber-Verlag, pp. 62–82.

Gambacorta G, Bersezio R, Weissert H and Erba E (2016) Onset and demise of Cretaceous oceanic anoxic events: the coupling of surface and bottom oceanic processes in two pelagic basins of the western Tethys. *Paleoceanography* **31**, 732–57.

Gibbons W and Moreno MT (eds) (2002) *The Geology of Spain*. Geological Society of London, 649 p.

Giorgioni M, Weissert W, Bernasconi SM, Hochuli PA, Cocción R and Séller CE (2012) Orbital control on carbon cycle and oceanography in the mid-Cretaceous greenhouse. *Paleoceanography* **27**, PA1204, https://doi.org/10.1029/2011PA002163.

Gledhill M and Buck KN (2012) The organic complexation of iron in the marine environment: a review. *Frontiers in Microbiology* **3**, 1–17.

Gómez-Alday JJ, López G and Elorza J (2004) Evidence of climatic cooling at the early/late Maastrichtian boundary from inoceramid distribution and isotopes: Sopelana sections, Basque Country, Spain. *Cretaceous Research* **25**, 649–68.

Gómez-Alday JJ, Zuluaga MC and Elorza J (2008) $^{87}Sr/^{86}Sr$ ratios in inoceramids (Bivalvia) and carbonate matrix as indicators of differential diagenesis during burial. Early Maastrichtian Bay of Biscay sections (Spain and France). Potencial use for chemostratigraphy? *Cretaceous Research* **29**, 563–76.

Heller MI, Lam PJ, Moffett JW, Till CP, Lee J-M, Toner BM and Marcus MA (2017) Accumulation of Fe oxyhydroxides in the Peruvian oxygen deficient zone implies non-oxygen dependent Fe oxidation. *Geochimica et Cosmochimica Acta* **211**, 174–93.

Hsü KJ and Jenkyns HC (1974) *Pelagic Sediments: On Land and Under the Sea*. Oxford: Blackwell Scientific Publication, 456 p.

Hu X, Jansa L, Wang C, Sarti M, Bak K, Wagreich M, Michalik J and Soták J (2005) Upper Cretaceous oceanic red beds (CORBs) in the Tethys: occurrences, lithofacies, age, and environments. *Cretaceous Research* **26**, 3–20.

Hu X, Scott RW, Cai Y, Wang C and Melinte-Dobrinescu MC (2012) Cretaceous oceanic red beds (CORBs): different time scales and models of origin. *Earth-Science Reviews* **115**, 217–48.

Hu X, Wang C, Scott RW, Wagreich M and Jansa L (eds) (2009) *Cretaceous Oceanic Red Beds: Stratigraphy, Composition, Origins, and Paleoceanographic and Paleoclimatic Significance*. Society of Economic Palaeontologists and Mineralogists, Special Publication no. 91, 276 p.

Huber BT, MacLeod KG, Watkins DK and Coffin MF (2018) The rise and fall of the Cretaceous Hot Greenhouse climate. *Global and Planetary Change* **167**, 1–23.

Hüneke H and Mulder T (2011) *Deep-sea Sediments*. Amsterdam: Elsevier, Developments in Sedimentology no. 63, 750 p.

Iridoy P, Zudaire S, Azaguirre M, Dorronsoro A, Olano G, Beriain E, Usarbarrena A and Elorza J (2010) Variaciones de color y contenido de $CaCO_3$ en los pares marga-caliza del Maastrichtiense superior y Eoceno inferior en Sopelana (Arco Vasco): reflejo de cambios paleoambientales. *Geogaceta* **49**, 91–4.

Jansa L and Hu X (2009) An overview of the Cretaceous pelagic black shales and red beds: origin, paleoclimate and paleoceanographic implications. In *Cretaceous Oceanic Red Beds: Stratigraphy, Composition, Origins, and Paleoceanographic and Paleoclimatic Significance* (eds X Hu, C Wang, RW Scott, M Wagreich and L Jansa), pp. 59–72. Society of Economic Palaeontologists and Mineralogists, Special Publication no. 91.

Jarvis I, Gale AS, Jenkyns HC and Pearce MA (2006) Secular variation in Late Cretaceous carbon isotopes: a new $\delta^{13}C$ carbonate reference curve for the Cenomanian–Campanian (99.6–70.6 Ma). *Geological Magazine* **143**, 561–608.

Jenkyns HC (1980) Cretaceous anoxic events: from continents to oceans. *Journal of the Geological Society of London* **137**, 171–88.

Jenkyns HC (2010) Geochemistry of oceanic anoxic events. *Geochemistry, Geophysics, Geosystems* **11**, Q03004, https://doi.org/10.1029/2009GC002788.

Jiménez Berrocoso Á, Elorza J and MacLeod KG (2013) Proximate environmental forcing in fine-scale geochemical records of calcareous couplets (Upper Cretaceous and Palaeocene of the Basque-Cantabrian Basin, eastern North Atlantic). *Sedimentary Geology* **284–285**, 76–90.

Jiménez Berrocoso Á, Zuluaga MC and Elorza J (2004) Minor- and trace-element intrashell variations in Santonian inoceramids (Basque-Cantabrian Basin, northern Spain): diagenetic and primary causes. *Facies* **50**, 35–60.

Jiménez Berrocoso Á, Zuluaga MC and Elorza J (2008) Diagenesis, palaeoclimate and tectono-sedimentary influences on clay mineralogy and stable isotopes from Upper Cretaceous marine successions of the Basque-Cantabrian Basin (N Spain). *Cretaceous Research* **29**, 386–404.

MacLeod KG (1994) Extinction of inoceramid bivalves in Maastrichtian strata of the Bay of Biscay region of France and Spain. *Journal of Paleontology* **68**, 1048–66.

MacLeod KG, Huber BT, Pletsch T, Röhl U and Kucera M (2001) Maastrichtian foraminiferal and paleoceanography changes on Milankovitch timescales. *Paleoceanography* **16**, 133–54.

MacLeod KG, Isaza Londoño C, Martin EE, Jiménez Berrocoso Á and Basak C (2011) Changes in the North Atlantic circulation at the end of the Cretaceous greenhouse. *Nature Geoscience* **4**, 779–82.

MacLeod KG and Ward PD (1990) Extinction pattern of Inoceramus (Bivalvia) based on shell fragment biostratigraphy. In *Global Catastrophes in Earth History* (eds VL Sharpton and PD Ward), pp. 509–518. Geological Society of America, Special Paper no. 247.

Mamet B and Préat A (2005) Why is "red marble" red? *Revista Española Micropaleontologia* **37**, 13–21.

Mamet B and Préat A (2006) Iron-bacterial mediation in Phanerozoic red limestones: state of the art. *Sedimentary Geology* **185**, 147–57.

Mamet B, Préat A and De Ridder Ch (1997) Bacterial origin of the red pigmentation in the Devonian Slivenec Limestone, Czech Republic. *Facies* **36**, 173–88.

Martín Chivelet J, Berástegui X, Rosales I, Vilas L, Vera JA, Caus E, Gräfe K-U, Mas R, Puig C, Segura M, Robles S, Floquet M, Quesada S, Ruiz-Ortiz PA, Fregenal-Martínez MA, Salas R, Arias C, García A, Martín Algarra A, Meléndez MN, Chacón B, Molina JM, Sanz JL, Castro JM, García-Hernández M, Carenas B, García-Hidalgo J, Gil J and Ortega F (2002) Cretaceous. In *The Geology of Spain* (eds W Gibbons and MT Moreno), pp. 255–292. Geological Society of London.

Mathey B (1982) El Cretácico Superior del Arco Vasco. In *El Cretácico de España* (ed. A García), pp. 111–135. Madrid: Universidad Complutense de Madrid.

Mathey B (1987) *Les flyschs Crétacé supérieur des Pyrénées Basques. Age, anatomie, origine du matériel, milieu de dépôt et relations avec l'ouverture du Golfe Gascogne*. Dijon: Université de Dijon, Mémoires Géologiques de l'Université de Dijon no. 12, 403 p.

Najarro M, Rosales I, Moreno-Bedmar JA, de Gea GA, Barrón E, Company M and Delanoy G (2011) High-resolution chemo- and biostratigraphic records of the Early Aptian oceanic anoxic event in Cantabria (N Spain):

palaeoceanographic and palaeoclimatic implications. *Palaeogeography, Palaeoclimatology, Palaeoecology* **299**, 137–58.

Noffke A, Hensen C, Sommer S, Scholz F, Bohlen L, Mosch T, Graco M and Wallmann K (2012) Benthic iron and phosphorus fluxes across the Peruvian oxygen minimum zone. *Limnology Oceanography* **57**, 851–67.

Ortega-Huertas M, Martínez-Ruiz F, Palomo I and Chamley H (1995) Comparative mineralogical and geochemical clay sedimentation in the Betic Cordilleras and Basque-Cantabrian Basin areas at the Cretaceous-Tertiary boundary. *Sedimentary Geology* **94**, 209–27.

Plaziat J-C (1981) Late Cretaceous to late Eocene palaeogeographic evolution of southwest Europe. *Palaeogeography, Palaeoclimatology, Palaeoecology* **36**, 263–320.

Préat A, De Ridder Ch and Gillan D (2018) Bacterial origin of the red pigmentation of Phanerozoic carbonate rocks: an integrated study of geology-biology-chemistry. *Geologica Belgica* **21**, 167–75.

Préat A, Morano S, Loreau J-P, Durlet C and Mamet B (2006) Petrography and biosedimentology of the Rosso Ammonitico Veronese (middle-upper Jurassic, north-eastern Italy). *Facies* **52**, 265–78.

Pujalte V, Baceta JI, Orue-Etxebarria X and Payros A (1998) Paleocene strata of the Basque Country, western Pyrenees, northern Spain; facies and sequence development in a deep-water starved basin. In *Mesozoic and Cenozoic Sequence Stratigraphy of European Basins* (eds PCh de Graciansky, J Hardenbol, T Jacquin and P Vail), pp. 311–325. Society of Economic Palaeontologists and Mineralogists, Special Publication no. 60.

Pujalte V, Robles S, Orue-Etxebarria X, Baceta JI, Payros A and Larruzea IF (2000) Uppermost Cretaceous-middle Eocene strata of the Basque-Cantabrian region and western Pyrenees: a sequence stratigraphic perspective. *Revista de la Sociedad Geológica de España* **13**, 191–211.

Raiswell R and Canfield D (2012) The iron biogeochemical cycle past and present. *Geochemical Perspectives* **1**, 1–220.

Rat P, Amiot M, Feuillee P, Floquet M, Mathey B, Pascal A and Salomón J (1983) *Vue sur le Crétacé Basco-Cantabrique et Nord-Ibérique*. Dijon: Université de Dijon, Mémoires Géologiques de l'Université de Dijon no. 9, 191 p.

Robinson SA, Dickson A, Pain A, Jenkyns H, O'Brien C, Farnsworth A and Lunt D (2019) Southern Hemisphere sea-surface temperatures during the Cenomanian–Turonian: implications for the termination of Oceanic Anoxic Event 2. *Geology* **47**, 131–4, https://doi.org/10.1130/G45842.1.

Robinson SA, Heimhofer U, Hesselbo SP and Petrizzo M-R (2017) Mesozoic climates and ocean – a tribute to Hugh Jenkyns and Helmut Weissert. *Sedimentology* **64**, 1–15, https://doi.org/10.1111/sed.12349.

Saltzman ES, Barron EJ and Price DA (1982) South Atlantic Cretaceous paleotemperatures from DSDP cores. *Palaeogeography, Palaeoclimatology, Palaeoecology* **40**, 167–81.

Sangüesa FJ, Arostegui J and Suarez-Ruiz I (2000) Distribution and origin of clay minerals in the Lower Cretaceous of the Alava Block (Basque-Cantabrian Basin, Spain). *Clay Minerals* **35**, 393–410.

Santander J, Sopelana A, Ramírez-Rodríguez JA, García-Peregrina I, Castaños J, Díez-López A, Perdigón O and Elorza J (2007) Contenido de $CaCO_3$ en los pares marga-caliza del Maastrichtiense y Daniense en Sopelana, Arco Vasco: facies grises frente a facies rojas. *Geogaceta* **43**, 95–8.

Schlanger SO and Jenkyns HC (1976) Cretaceous oceanic anoxic events: causes and consequence. *Geologie en Mijnbouw* **55**, 179–84.

Scholle PA and Arthur MA (1980) Carbon isotope fluctuations in Cretaceous pelagic limestones: potential stratigraphic and petroleum exploration tool. *AAPG Bulletin* **64**, 67–87.

Scott R (2009) Chronostratigraphic database for Upper Cretaceous oceanic red beds (CORBs). In *Cretaceous Oceanic Red Beds: Stratigraphy, Composition, Origins, and Paleoceanographic and Paleoclimatic Significance* (eds X Hu, C Wang, RW Scott, M Wagreich and L Jansa), pp. 35–57. Society of Economic Palaeontologists and Mineralogists, Special Publication no. 91.

Skupien P, Bubík M, Svábenická L, Mikulás R, Vasícek Z and Matysek D (2009) Cretaceous oceanic red beds in the outer Western Carpathian, Czech Republic. In *Cretaceous Oceanic Red Beds: Stratigraphy, Composition, Origins, and Paleoceanographic and Paleoclimatic Significance* (eds X Hu, C Wang, RW Scott, M Wagreich and L Jansa), pp. 99–109. Society of Economic Palaeontologists and Mineralogists, Special Publication no. 91.

Song H, Jiang G, Poulton SW, Wignall PB, Tong J, Song H, An Z, Chu D, Tian L, She Z and Wang C (2017) The onset of widespread marine red beds and the evolution of ferruginous oceans. *Nature Communications* **8**, 399, https://doi.org/10.1038/s41467-017-00502-x.

Stow DAV (2005) *Sedimentary Rocks in the Field*. London: Manson Publishing Ltd, 320 p.

Tucker ME (1994) *Sedimentary Petrology: An Introduction to the Origin of Sedimentary Rocks*. London: Blackwell Scientific Publication, Second Edition, 260 p.

Tyrell GW (1926) *The Principles of Petrology; An Introduction to the Science of Rocks*. London: Methuen Publishing, 349 p.

Van der Kooij B, Immenhauser A, Steuber T, Hagmaier M, Bahamonde JR, Samankassou E and Merino Tomé O (2007) Marine red staining of a Pennsylvanian carbonate slope: environmental and oceanographic significance. *Journal of Sedimentary Research* **77**, 1026–45.

Vera JA (2004) *Geología de España*. Madrid: SGE-IGME, 890 p.

Wagreich M and Krenmayr H-G (2005) Upper Cretaceous oceanic red beds (CORB) in the Northern Calcareous Alps (Nierental Formation, Austria): slope topography and clastic input as primary controlling factors. *Cretaceous Research* **26**, 57–64.

Wagreich M, Neuhuber S, Egger H, Wendler I, Scott R, Malata E and Sanders D (2009) Cretaceous oceanic red beds (CORBs) in the Austrian Alps: passive margin vs. active-margin depositional settings. In *Cretaceous Oceanic Red Beds: Stratigraphy, Composition, Origins, and Paleoceanographic and Paleoclimatic Significance* (eds X Hu, C Wang, RW Scott, M Wagreich and L Jansa), pp. 73–88. Society of Economic Palaeontologists and Mineralogists, Special Publication no. 91.

Wang C, Hu X, Huang YJ, Scott RW and Wagreich M (2009) Overview of Cretaceous oceanic red beds (CORBs): a window on global oceanic and climate change. In *Cretaceous Oceanic Red Beds: Stratigraphy, Composition, Origins, and Paleoceanographic and Paleoclimatic Significance* (eds X Hu, C Wang, RW Scott, M Wagreich and L Jansa), pp. 13–33. Society of Economic Palaeontologists and Mineralogists, Special Publication no. 91.

Wang C, Hu X, Huang Y, Wagreich M, Scott R and Hay W (2011) Cretaceous oceanic red beds as possible consequence of oceanic anoxic events. *Sedimentary Geology* **235**, 27–37.

Wang C, Hu X, Sarti M, Scott RW and Li X (2005) Upper Cretaceous oceanic red beds in southern Tibet: a major change from anoxic to oxic, deep-sea environments. *Cretaceous Research* **26**, 21–32.

Wang C, Huang Y, Hu X and Li X (2004) Cretaceous oceanic redbeds: implications for paleoclimatology and paleoceanography. *Acta Geologica Sinica (English Edition)* **78**, 873–7.

Ward PD and Kennedy WJ (1993) Maastrichtian ammonites from the Biscay region (France, Spain). *Journal of Paleontology* **34**, 1–58.

Ward PD, Kennedy WJ, MacLeod KG and Mount J (1991) End-Cretaceous molluscan extinction patterns in Bay of Biscay K/T boundary sections, two different patterns. *Geology* **19**, 1181–4.

Weissert H, McKenzie JA and Channell JET (1985) Natural variations in the carbon cycle during the Early Cretaceous. In *The Carbon Cycle Atmospheric CO2: Natural Variations Archean to Present* (eds ET Sundquist and WS Broecker), pp. 531–545. Washington, DC: AGU, Geophysical Monograph Series no. 32.

Wilson PA and Norris RD (2001) Warm tropical ocean surface and global anoxia during the Mid-Cretaceous period. *Nature* **412**, 425–9.